In: Geoinformatics for Natural Resource Management
Editors: P.K. Joshi, P. Pani, S.N. Mohapatra et al.
ISBN: 978-160692-211-8

Chapter 19

GEOINFORMATICS FOR URBANISATION AND URBAN SPRAWL PATTERN ANALYSIS

T. V. Ramachandra [*] ***and Uttam Kumar*** [†]
Centre for Ecological Sciences, Indian Institute of Science
Centre for Sustainable Technologies, Indian Institute of Science

ABSTRACT

Urbanisation is the increase in the population of cities in proportion to the region's rural population. Bangalore is experiencing unprecedented urbanisation in recent times due to concentrated developmental activities with impetus on industrialization for the economic development of the region. This concentrated growth has resulted in the increase in population and consequent pressure on infrastructure, natural resources and ultimately giving rise to a plethora of serious challenges such as climate change, global warming, green-house effect, etc. This trend due to burgeoning population has posed serious challenges to the decision makers in the city planning and management process involving plethora of issues like infrastructure development, traffic congestion, and basic amenities (electricity, water, and sanitation), etc. In this context, to aid the decision makers in following the holistic approaches in the city and urban planning, the pattern, analysis, visualization of urban growth and its impact on natural resources has gained importance. This communication, analyses the urbanisation pattern and trends using temporal remote sensing data based on supervised learning using maximum likelihood estimation of multivariate normal density parameters and Bayesian classification approach. The technique is implemented with Landsat data of 1973, 1992 and 2000, IRS LISS-3 data of 1999, 2006 and MODIS data of 2002 and 2007. The study shows that there has been a growth of 466% in urban areas of Greater Bangalore across 35 years (1973 to 2007). The study unravels the pattern of growth in Greater Bangalore and its implication on local climate and also on the natural resources, necessitating appropriate strategies for the sustainable management.

Key words: Bangalore, geoinformatics, LISS, MODIS, sprawl, urbaninsation

[*] http://wgbis.ces.iisc.ernet.in/energy; Email: cestvr@ces.iisc.ernet.in
[†] Email-uttam@ces.iisc.ernet.in

INTRODUCTION

Urbanisation is a form of metropolitan growth that is a response to often bewildering sets of economic, social, and political forces and to the physical geography of an area. This could be planned (like townships, etc.) or unplanned (organic). Many organic cities are now undergoing redevlopment for economic purposes with new roads, infrastructure improvements, etc. It results in the increase in population in proportion to the region's rural population. This phenomenona is very rapid in India with urban population growing at around 2.3 percent per annum. The 20th century is witnessing "the rapid urbanisation of the world's population", as the global proportion of urban population rose dramatically from 13% (220 million) in 1900, to 29% (732 million) in 1950, to 49% (3.2 billion) in 2005 and is projected to rise to 60% (4.9 billion) by 2030 (World Urbanisation Prospects, 2005). An increased urban population and growth in urban areas is inadvertent with population growth and migration. There are 35 urban agglomerations/cities having a population of more than one million in India (in 2001). Of the 4000 plus urban agglomerations, about 38 percent reside in just 35 urban areas, thus indicating the magnitude of urbanisation. Overall rise in population of urban poor or increase in travel times owing to congestion in road networks are indicators of the performance of planning in assessing and catering to the demand and lack of good urban governance. Thus the administration at all levels: local bodies, state government and national government are facing the brunt of rapid urban growth. It is imperative for planning and governance to facilitate, augment and service the requisite infrastructure over time systematically. This requires an understanding of pattern of urbanisation dynamics with causal factors. Traditional urbanisation exhibits a concentration of human activities and settlements around the regions of economic activities. With respect to the role of technology in urbanisation, Berry (1990) has illustrated a new linkage between transport infrastructure development cycles and spurts in urbanisation. Urban infrastructure development is unlikely to keep pace with urban population growth. Both local environmental impacts, such as deterioration of water quality in streams and an increased potential for harbouring disease vectors, and offsite land cover changes, such as the loss of woodland and forest to meet urban fuel wood demands, are likely to occur (Douglas, 1994). The direct implication of such urbanisation is the change in land use and land cover of the region. Urban ecosystems are the consequence of the intrinsic nature of humans as social beings to live together (Sudhira *et al.*, 2003). The process of urbanisation contributed by infrastructure initiatives and consequent population growth and migration results in the growth of villages into towns, towns into cities and cities into metros. However, in such a phenomenon for ecologically feasible development, planning requires an understanding of the growth dynamics. Nevertheless, in most cases there are lot of inadequacies to ascertain the nature of uncontrolled progression of urban sprawls.

Urban sprawl refers to the dispersed development along highways or surrounding the city and in rural countryside with implications such as loss of agricultural land, open space and ecologically sensitive habitats. Sprawl is thus a pattern and pace of land use in which the rate of land consumed for urban purposes exceeds the rate of population growth resulting in an inefficient and consumptive use of land and its associated resources. This phenomenon is characterized by an unplanned and uneven pattern of growth, driven by multitude of processes evident from lack of basic amenities. Urban sprawl is thus a term often used

variously to mean the gluttonous use of land, uninterrupted monotonous development, leapfrog discontinuous development and inefficient use of land that are influenced by a myriad of factors, including land features, infrastructure, policies, and individual characteristics. This is characterised by low levels of some combination of eight distinct dimensions such as density, continuity, concentration, clustering, centrality, nuclearity, mixed uses and proximity (Elena and Nancy, 2004; Galster *et al.*, 2001; Peiser, 2001; Ramachandra *et al.*, 2004). Basic spatial forms of sprawl are described by Low-density sprawl, Ribbon and Leapfrog development. The consumptive use of land for urban purposes along the margins of existing metropolitan area supported by piecemeal extensions of basic urban infrastructures such as water, sewer, power and roads characterizes low-density sprawl. The development that follows major transportation corridors outward from urban cores with lands adjacent to corridors are developed, but those without direct access remain in rural uses/covers characterizes ribbon sprawl. Over time these nearby raw lands may be converted to urban uses as land values increase and infrastructure is extended perpendicularly from the major roads and lines. Provision of certain infrastructure facilities like new roads and highways, fuel such sprawls that ultimately result in inefficient and drastic change in land use affecting the ecosystem. Compared to these, leapfrog development is a discontinuous pattern of urbanisation, with patches of developed lands that are widely separated from each other and from the boundaries. This form of development would be expensive for providing urban services such as treated drinking water supply, provision of electricity, waste and sewerage (http://chesapeake.towson.edu/landscape/urbansprawl).

Consequences of Urbanisation and Urban Sprawl

Urbanisation and urban sprawl have posed serious challenges to the decision makers in the city planning and management process involving plethora of issues like infrastructure development, traffic congestion, and basic amenities (electricity, water, and sanitation), etc. (Kulkarni and Ramachandra, 2006). Apart from this, major implications of urbanisation are:

- **Floods:** Common consequences of urban development are increased peak discharge and frequency of floods as land is converted from fields or woodlands to roads and parking lots, it loses its ability to absorb rainfall. Conversion of water bodies to residential layouts has compounded the problem by removing the interconnectivities in an undulating terrain.
- **Heat island:** Surface and atmospheric temperatures are increased by anthropogenic heat discharge due to energy consumption, increased land surface coverage by artificial materials having high heat capacities and conductivities, and the associated decreases in vegetation and water pervious surfaces, which reduce surface temperature through evapotranspiration.
- **Loss of aquatic ecosystems:** Urbanisation has telling influences on the natural resources evident from the sharp decline in number of water bodies and also from depleting groundwater table. Figure 1 illustrates the loss of aquatic ecosystems (70% decline during 1973-2007 in the Bangalore city limits) and vegetation with the increase in built up area (466% during 1973-2007).

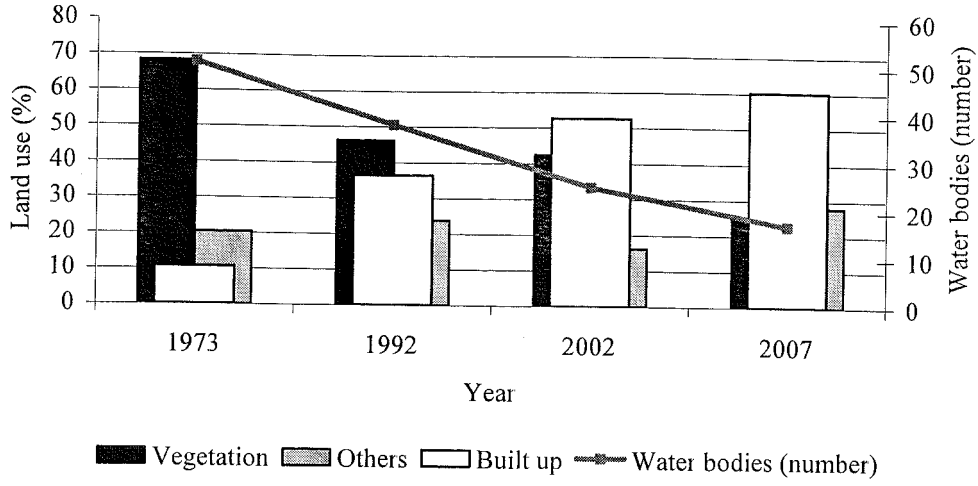

Figure 1. Temporal changes in built up and its impact on vegetation and water bodies

Problem Identification

Sprawl is perceived as one of the potential threats for development as the biggest confront is to ensure adequate housing with basic infrastructure and amenities including health, sanitation, etc. Currently, sprawl regions are devoid of any infrastructure, since planners are unable to visualize this type of growth patterns. This growth is normally not accounted in all government surveys (even in national population census), as these pockets are grouped either under urban or rural. The investigation of patterns of this kind of growth is very crucial from regional planning point of view to provide basic amenities (Ramachandra *et al.*, 2004). Prior visualizing of the trends and patterns of growth enable the planning machineries to plan for appropriate basic infrastructure facilities (water, electricity, sanitation, etc.). Also, by 2050 over 6 billion people, two thirds of humanity, will be living in towns and cities. This necessitates understanding the type, extent and nature of sprawl taking place in a region. In this regard, temporal remote sensing data aids in capturing the spatial growth patterns and process. Remote sensing coupled with geospatial analysis aid greatly in monitoring and management of the urbanisation process. The spectral pattern present within the remote sensing data for each pixel is used to perform the classification and, indeed, is used as the numerical basis for categorization of various spatial features (Lillesand *et al.*, 2002). Identifying, delineating and mapping urban areas on temporal scale provide an opportunity to monitor the changes, which is important for natural resource management and sustainable planning activities. Geospatial system helps in the integration of remotely sensed classified data and ancillary information from various other sources (population, natural resources, etc.) to arrive at decisions related to development of urban growth.

In this work, Landsat data of 1973 (of 79 m spatial resolution), 1992 and 2000 (30 m), IRS LISS-3 data of 1999 and 2006 (23.5 m) and MODIS data of 2002 and 2007 (with 250 m to 500 m spatial resolution) are used with supervised pattern classifiers based on maximum

likelihood (ML) estimation followed by a Bayesian statistical approach. This technique quantifies the tradeoffs between various classification decisions using probability and costs that accompany such decisions (Duda *et al.*, 2000). It makes assumptions that the decision problem is posed in probabilistic terms, and that all of the relevant probability values are known with a number of design samples or training data collected from field that are particular representatives of the patterns to be classified. The mean and covariance are computed using maximum likelihood estimation with the best estimates that maximizes the probability of the pixels falling into one of the classes. Also, an attempt is made to map land surface temperatures across various land cover types to understand heat island effect. Urban Heat Island (UHI) studies have traditionally been conducted for isolated locations and with in situ measurements of air temperatures. The advent of satellite remote sensing technology has made it possible to study UHI both remotely and on continental or global scales (Streutker, 2002).

Review of Literature

Recent interest in the analysis and monitoring of urban landscapes using remote sensing data has led to the development of a number of classification methodologies. Urban growth pattern has been studied by Masser and Cheng (2003), Rawashdeh and Saleh (2006), etc. Guindon *et al.*, (2004) generated two independent land cover products, one spectral-based at the pixel level and the other segment-based using Landsat Thematic Mapper (TM). These classifications were then merged through a rule-based approach to generate a final product with enhanced land use classes with producer accuracies of 78% and 73%. Spatio temporal dynamics for urban sprawl has also been reported (Tian *et al.*, 2005; Yu and Ng, 2007). Most of these studies have been carried out with high spatial resolution data at the micro level such as individual building mapping, road extraction etc. (Barnsley and Barr, 1997; Barr and Barnsley, 2000; Mesev, 2005) and are based on pattern recognition techniques involving supervised or unsupervised classification. Among the various frameworks in which pattern recognition has been traditionally formulated, the statistical approach has been most intensively studied and used in practice.

More recently, neural network techniques and methods based on the statistical learning theory have received increasing attention. The design of a recognition system also involves definition of pattern classes, sensing environment, pattern representation, feature extraction and selection, cluster analysis, classifier design and learning, selection of training and test samples and performance evaluation. Pattern recognition techniques such as neural network, decision tree, fuzzy theory etc. have been widely used with remote sensing data to identify the patterns in land use classes like urban, agriculture land, etc. (Kwan *et al.*, 1994; Fukushima *et al.*, 1998; Gori *et al.*, 1998; Lee *et al.*, 2006). Both conventional thresholding strategy such as NDVI (Masek *et al.*, 2000) and customized indices such as the Normalized Built-up Indicator (Zha *et al.*, 2003) have been used to segregate urban from non-urban lands. Ridd (1995) while studying ecosystem aspects of Salt Lake City, USA proposed viewing urban pixels as being composed of linear combinations of three generic land cover components, vegetation, impervious surface and soil (V–I–S model). This technique was applied later to Brisbane, Australia (Phinn *et al.*, 2002) and Cairo, Egypt (Rashed *et al.*, 2001). Operational impervious surface mapping methods have also been developed at the United States Geological Survey

(Yang *et al.*, 2003). Percent impervious surface is currently being used as a measure of urban intensity as part of the Landsat-based 2001 National Land Cover Dataset (Homer *et al.*, 2002). Other approaches have attempted to exploit attributes of image spatial features to delineate urban areas, namely, the density and regularity of these features. Measures of image texture, i.e. radiometric variability, have been suggested (Moller-Jensen, 1990; Gluch, 2002; Arumugam *et al.*, 2003). Gong and Howarth (1990) applied edge detection and smoothing techniques to generate a spatial pseudospectral road-density band to augment conventional spectral bands in classification. Zhang *et al.* (2003) applied a similar approach to study urban change in Beijing. In this case, instead of edge, line detection was applied since the latter better conforms to road patterns (Wang, 1993).

The general problem of recognising complex data patterns with arbitrary orientation, location, and scale still present challenges. For example, coarse spatial resolution data acquired from MODIS Aqua/Terra with 250 m to 1 km presents identification and pattern classification challenges for urban pixels since most of the pixels would represent signatures that are combination of various types of urban entities reflectance. These include spectral mixing of diverse land cover components within pixels, spectral confusion with other land cover features such as fallow, agricultural fields and the fact that urban classes of interest are of the land use and not the land cover category. There are various techniques that can be used to improve the spatial resolution of the images including image fusion, resampling, principal component, etc. Once the image is classified, with the details of land features of interest from remotely sensed data, it becomes useful to the regional decision makers to management planners. In this context, study of urban growth from temporal satellite imageries are required for monitoring their status, extent across time, which give insights into many other underlying processes and issues.

Urbanisation drastically alters the drainage characteristics of natural catchments, or drainage areas, by increasing the volume and rate of surface runoff. Drainage systems are unable to cope with the increased volume of water and are often encountered with the blockage due to indiscriminate disposal of solid wastes. Encroachment of wetlands, floodplains, etc. obstructs floodways causing loss of natural flood storage. Konig *et al.*, (2002) divided damages from urban flooding into two categories:

- Direct damage—typically material damage caused by water or flowing water.
- Indirect damage—social consequences that are negative long term effects of a more psychological character, like decrease of property values in frequently flooded areas and delayed economical development, for e.g. traffic disruptions, administrative and labour costs, production losses, spreading of diseases, etc.

Urban flooding creates considerable infrastructure problems and huge economic losses in terms of production, as well as significant damage to property and goods. Flooding in urban areas causes large damage at buildings and other public and private infrastructure. Besides, street flooding can limit or completely hinder the functioning of traffic systems and has indirect consequences such as loss of business and opportunity. The expected total damage; direct and indirect monetary damage costs as well as possible social consequences is related to the physical properties of the flood, i.e. the water level above ground level, the extend of flooding in terms of water volume escaping from or not being entering the drainage system,

and the duration of flooding. With sloped surfaces even the flow velocity on the surface might have an impact on potential flood damage (Schmitt *et al.*, 2002).

The main hydrologic parameters that are used to represent urbanisation are (a) impermeable area that is the proportion of the surface area for which precipitation enters the storm-water network directly and (b) time of concentration or velocity of the flow through the basin (Campana *et al.*, 2001). SCS model (U.S. Soil Conservation Service, 1972; Shi *et al.*, 2007) incorporates the parameter CN (runoff potential) to estimate the overland flow volume based on soil type and urban development characteristics like plot size in residential, commercial and industrial areas, among others. Campana and Tucci (1994) used fuzzy mathematics to estimate the impermeable areas from Landsat-TM images of urban developments in Brazil. They used data from the cities of Sao Paulo, Curitiba and Porto Alegre (population, 16, 2.5 and 3 million inhabitants) to establish a relationship between urban density and impermeable area. The time of concentration, or time to hydrograph peak, of an urban basin is usually obtained by empirical equations or by using equations established for rural basins (Diaz and Tucci, 1987; Porto *et al.*, 1993). These equations are useful, as a first approximation, but do not satisfactorily describe all local conditions. The time of concentration of a basin can be considered as made up of two components; the time taken by overland flow from the basin headwaters to reach the drainage system, and time spent in the runoff channels (Campana *et al.*, 2001).

Studies using satellite-derived radiant temperature have been termed as the surface temperature heat islands (Streutker, 2002). The phenomenon of UHI using satellite derived land surface temperature (LST) measurements have been conducted using various satellite data products acquired in thermal region of the electromagnetic spectrum. Currently available satellite thermal infrared sensors provide different spatial resolution and temporal coverage data that can be used to estimate LST. The Geostationary Operational Environmental Satellite (GOES) has a 4-km resolution in the thermal infrared, while the NOAA-Advanced Very High Resolution Radiometer (AVHRR) and the Terra and Aqua-MODIS have 1-km spatial resolutions. Significantly high resolution data come from the Terra-Advanced Spaceborne Thermal Emission and Reflection Radiometer (ASTER) which has a 90 m pixel resolution, the Landsat-5 Thematic Mapper (TM) which has a 120 m resolution, and Landsat-7 Enhanced Thematic Mapper (ETM) which has a 60 m resolution. However, these instruments have a repeat cycle of 16 days (Li *et al.*, 2004).

NOAA AVHRR data were used to derive LST for studying heat island phenomenon (Balling and Brazell, 1988; Gallo *et al.*, 1993; Gallo and Owen, 1998; Kidder and Wu, 1987, Roth *et al.*, 1989; Streutker, 2002). The 1.1-km spatial resolution of these data is found suitable only for small-scale urban temperature mapping. The 120 m spatial resolution Landsat TM Thermal Infrared (TM TIR) data have also been utilized to derive surface temperatures. Carnahan and Larson (1990) used TM TIR data to observe meso-scale temperature differences between the urban and the rural area in Indianapolis. Tanaka *et al.*, (2005) used Landsat TM data to study the characteristics of heat island phenomenon. Nichol (1994) carried out a detailed study using TM thermal data to monitor microclimate for housing estates in Singapore. Weng (2001, 2003) examined LST pattern and its relationship with land cover in Guangzhou and in the urban clusters in the Zhujiang Delta, China. Kato and Yamaguchi, (2005) have used ASTER and ETM+ data for analysis of urban heat island. Nikolakopopulos *et al.*, (2003) have used Landsat-5 TM and Landsat-7 ETM+ data for creating the temperature profile of Alfios River Basin. Stathopoulou and Cartalis (2007) have

used Landsat ETM+ data to identify daytime urban heat island using Corine land cover data for major cities in Greece. Using a Landsat ETM+ imagery of City of Indianapolis, IN, USA, Weng *et al.*, (2004) examined the surface temperature UHI in the city. They derived LST and analysed their spatial variations using Landsat ETM+ thermal measurements with the urban vegetation abundance and investigated their relationship.

LST is believed to correspond more closely with the UCL (Upper Canopy Layer) heat islands, although a precise transfer function between LST and the near-ground air temperature is not yet available (Nichol, 1994). Research on LST shows that the partitioning of sensible and latent heat fluxes and thus surface radiant temperature response is a function of varying surface soil water content and vegetation cover (Owen *et al.*, 1998). A higher level of latent heat exchange was found with more vegetated areas, while sensible heat exchange was more favored by sparsely vegetated, such as urban areas (Oke, 1982). This relationship between LST and vegetation abundance (e.g., Carson *et al.*, 1994; Gallo and Owen, 1998; Gillies and Carlson, 1995; Gillies *et al.*, 1997; Goward *et al.*, 2002; Lo *et al.*, 1997; Weng, 2001), and the relationship to derive biophysical parameters (Carson *et al.*, 1994; Gillies and Carlson, 1995; Gillies *et al.*, 1997) aid primarily in land cover mapping and change analysis (Lambin and Ehrlich, 1996; Sobrino and Raissouni, 2000).

Satellite TIR sensors measure top of the atmosphere (TOA) radiances, from which brightness temperatures (also known as blackbody temperatures) can be derived (Dash *et al.*, 2002). The TOA radiances are the mixing result of emitted radiance from the Earth's surface, upwelling radiance from the atmosphere, and downwelling radiance from the sky. The difference between the TOA and land surface brightness temperatures ranges generally from 1 to 5 K in the 10–12 μm spectral region, subject to the influence of the atmospheric conditions (Prata *et al.*, 1995). Therefore, atmospheric effects, including absorption, upward emission, and downward irradiance reflected from the surface (Franca and Cracknell, 1994), must be corrected before land surface brightness temperatures are obtained. These brightness temperatures should be further corrected with spectral emissivity values prior to the computation of LST to account for the roughness properties of the land surface, the amount and nature of vegetation cover, and the thermal properties and moisture content of the soil (Friedl, 2002). Two approaches have been developed to recover LST from multispectral TIR imagery (Schmugge *et al.*, 1998). The first approach utilizes a radiative transfer equation to correct the at-sensor radiance to surface radiance, followed by an emissivity model to separate the surface radiance into temperature and emissivity (Schmugge *et al.*, 1998). The second approach applies the split-window technique for sea surfaces to land surfaces, assuming that the emissivity in the channels used for the split window is similar (Dash *et al.*, 2002). Land surface brightness temperatures are then calculated as a linear combination of the two channels. A major disadvantage of this approach is that the coefficients are only valid for the data sets used to derive them (Dash *et al.*, 2002). In other words, a set of thermal responses for a specific landscape phenomenon or process measured using a specific TIR sensor cannot be extrapolated to predict the same TIR measurements either from other sensors, or from images recorded at different times using the same sensor (Quattrochi and Goel, 1995).

Estimation of emissivities for ground objects from passive sensor data has been measured using different techniques including the normalized emissivity method (Gillespie, 1985), thermal spectral indices (Becker and Li, 1990), spectral ratio method (Watson, 1992), Alpha residual method (Kealy and Gabell, 1990), NDVI method (Valor and Caselles, 1996), classification-based estimation (Snyder *et al.*, 1998), and the temperature emissivity

separation method (Gillespie *et al.*, 1998). These techniques are also useful to separate temperatures from emissivities. Lack of knowledge of emissivity can introduce an error ranging from 0.2 to 1.2 K for mid-latitude summers and from 0.8 to 1.4 K for the winter conditions for an emissivity of 0.98 and at the ground height of 0 km, when a single channel method of LST estimation is used (Dash *et al.*, 2002). Moreover, it may not be practical to measure emissivity values pixel-by-pixel, since numerous factors are involved. Snyder *et al.* (1998) proposed to use kernel methods applied to three bidirectional reflectance distribution function (BRDF) models (a geometric model for sparse vegetation, a volumetric model for dense vegetation, and a specular model for water and ice), so that each pixel can be categorized into 1 of the 14 emissivity classes based on conventional land cover classification and dynamic and seasonal factors.

The basis for using NDVI in LST estimation is that the amount of vegetation present is an important factor and NDVI is used to infer general vegetation conditions. The combination of LST and NDVI by scatter plot results in a triangular shape (Carson *et al.*, 1994; Gillies and Carlson, 1995; Gillies *et al.*, 1997). The slope of the LST–NDVI curve has been related to soil moisture conditions (Carson *et al.*, 1994; Gillies and Carlson, 1995; Gillies *et al.*, 1997; Goetz, 1997; Goward *et al.*, 2002), and the evapo-transpiration of the surface (Boegh *et al.*, 1998). Several methods have been developed to interpret the LST–NDVI space, including: (1) the triangle method using soil–vegetation–atmosphere transfer (SWAT) model (Carson *et al.*, 1994; Gillies and Carlson, 1995; Gillies *et al.*, 1997); (2) in situ measurement method (Friedl and Davis, 1994); and (3) remote sensing based method (Betts *et al.*, 1996). However, difficulties still exist in interpretation of LST for sparse canopies because the measurements have combined the temperature of the soil and that of the vegetation, and the combinations are often nonlinear (Sandholt *et al.*, 2002). Interpreting thermal data and images of temperature distribution over an area is often not easy because of many complex factors involved. The most influential factors for controlling the UCL heat island are the distribution of surface cover characteristics, and urban morphology, such as building materials, geometry, and density (Oke, 1982). Each component surface in urban landscapes exhibits a unique radiative, thermal, moisture, and aerodynamic properties, and relates to their surrounding site environment. The myriad of the component surfaces and the spatial complexity, when mosaicked create a limitless array of energy balance and microclimate systems, confiscating urban meteorologists from drawing any generalization (Oke, 1982).

Study Area

Greater Bangalore (77°37'19.54'' E and 12°59'09.76'' N) is the principal administrative, cultural, commercial, industrial, and knowledge capital of the state of Karnataka with an area of 741 sq km and lies between the latitudes 12°39'00'' to 131°3'00''N and longitude 77°22'00'' to 77°52'00''E. Bangalore city administrative jurisdiction was widened in 2006 by merging the existing area of Bangalore city spatial limits with 8 neighbouring Urban Local Bodies (ULBs) and 111 Villages of Bangalore Urban District (Sudhira *et al*, 2007). Thus, Bangalore has grown spatially more than ten times since 1949 (69 sq km) and is a part of both the Bangalore urban and rural districts (Fig. 3). Now, Bangalore is the fifth largest metropolis in India currently with a population of about 7 million (Fig. 2).

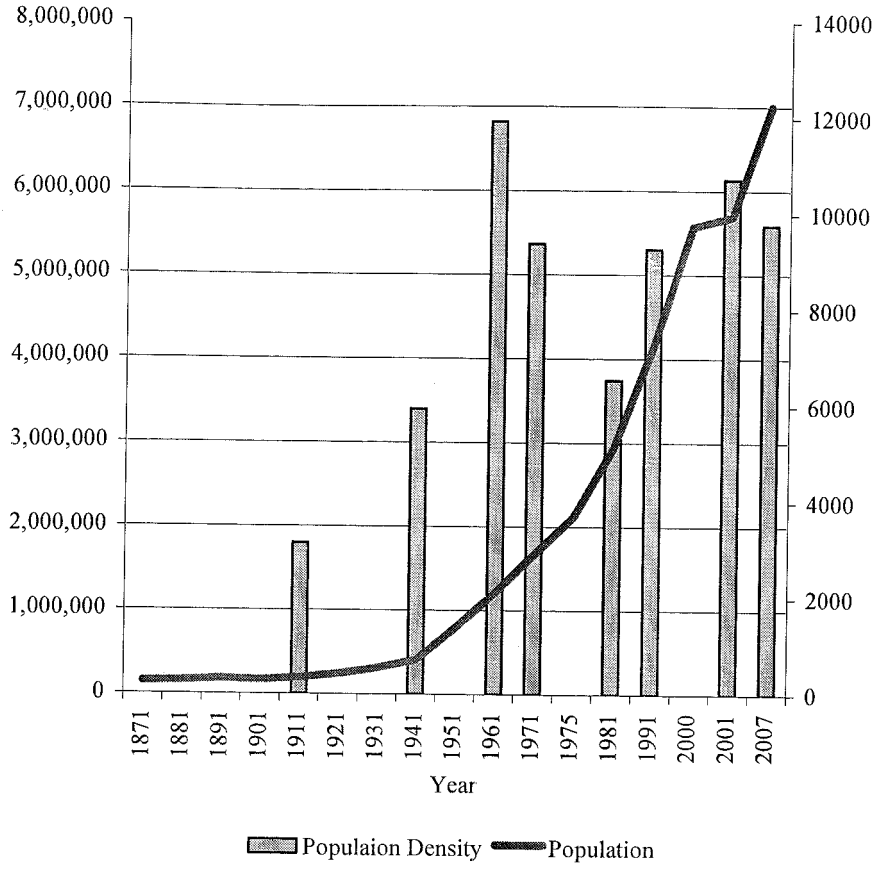

Figure 2. Population growth and population density

The mean annual total rainfall is about 880 mm with about 60 rainy days a year over the last ten years. The summer temperature ranges from 18° C – 38° C, while the winter temperature ranges from 12° C – 25° C. Thus, Bangalore enjoys a salubrious climate all round the year. Bangalore is located at an altitude of 920 m above mean sea level, delineating four watersheds, viz. Hebbal, Koramangala, Challaghatta and Vrishabhavathi watersheds. The undulating terrain in the region has facilitated creation of a large number of tanks providing for the traditional uses of irrigation, drinking, fishing and washing. This led to Bangalore having hundreds of such water bodies through the centuries. Even in early second half of 20th century, in 1961, the number of lakes and tanks in the city stood at 262 (and spatial extent of Bangalore was 112 sq km). However, number of lakes and tanks in 1985 was 81 (and spatial extent of Bangalore was 161 sq km).

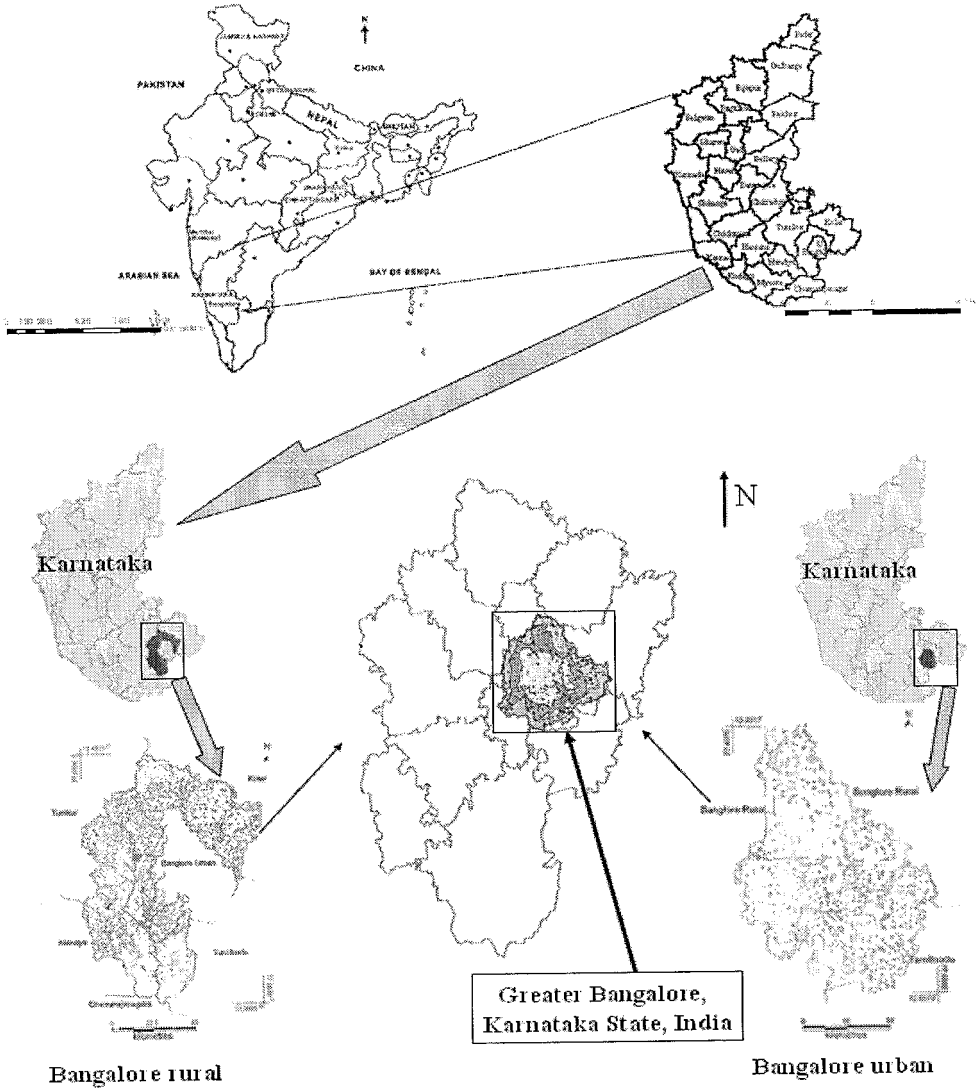

Figure 3. Study area – Greater Bangalore

MATERIALS AND METHODS

Survey of India (SOI) toposheets of 1:50000 and 1:250000 scales were used to generate base layers of taluk boundaries, city boundary, drainage networks, and water bodies. Field data were collected with a handheld GPS. Remote sensing data (spatial and spectral resolutions are listed in table 1) used for the study are:

- Landsat MSS of 1973 [downloaded from http://glcf.umiacs.umd.edu/data/]
- Landsat TM of 1992 [downloaded from http://glcf.umiacs.umd.edu/data/]
- Landsat ETM+ of 2000 [downloaded from http://glcf.umiacs.umd.edu/data/]

- IRS (Indian Remote Sensing) LISS (Linear Imaging Self Scanner)-III of 1999 and 2006
- MODIS (Moderate Resolution Imaging Spectroradiometer) Surface Reflectance 7 bands product [downloaded from http://edcdaac.usgs.gov/main.asp] of 2002 and 2007
- MODIS Land Surface Temperature/Emissivity 8-Day L3 Global and Daily L3 Global (V004 and V005 products)
- [downloaded from http://lpdaac.usgs.gov/modis/dataproducts.asp#mod11]
- SRTM (Shuttle Radar Topography Mission) elevation data of 90 m resolution [downloaded from http://glcf.umiacs.umd.edu/data/] and
- Google Earth image (http://earth.google.com) served in pre and post classification process and validation of the results.

Table 1. Spatial and spectral details of the remote sensing data used for analysis

Sensors/ Data Products	Band Number	Sensitivity (μm)	Resolution (m)	Year of acquisition
Landsat MSS	1	0.5 – 0.6	79	1973
	2	0.6 – 0.7	79	
	3	0.7 – 0.8	79	
	4	0.8 – 1.1	79	
Landsat TM	1	0.45 – 0.52	30	1992
	2	0.52 – 0.60	30	
	3	0.63 – 0.69	30	
	4	0.76 – 0.90	30	
	6	10.4 – 12.5	120 (TIR)	
Landsat ETM+	2	0.525 – 0.605	30	2000
	3	0.630 – 0.690	30	
	4	0.750 – 0.900	30	
	5	1.55 – 1.75	30	
	6	10.44 – 12.42	60 (TIR)	
	7	2.09 – 2.35	30	
	8	520 – 0.900	15 (PAN)	
IRS LISS-3 MSS	1	0.52 – 0.59	23.5	1999 and 2006
	2	0.62 – 0.68	23.5	
	3	0.77 – 0.86	23.5	
MODIS Surface Reflectance 8-Day L3 Global	1	620 – 670	250	2002 and 2007
	2	841 – 876	250	
	3	459 – 479	500	
	4	545 – 565	500	
	5	1230 – 1250	500	
	6	1628 – 1652	500	
	7	2105 – 2155	500	
MODIS Land Surface Temperature/Emissivity 8-Day L3 Global	1	11.770-12.270	1000	2000 and 2007

Methods

The methods adopted in the analysis involved:

Creation of base layers: Base layers like district boundary, district with taluk and village boundaries, road network, drainage network, mapping of water bodies, etc. from the SOI toposheets of scale 1:250000 and 1:50000.

Georeferencing of acquired remote sensing data to latitude-longitude coordinate system with Evrst 56 datum: Landsat bands, IRS LISS-III MSS bands, MODIS bands 1 and 2 (spatial resolution 250 m) and bands 3 to 7 (spatial resolution 500 m) were geocorrected with the known ground control points (GCP's) and projected to Polyconic with Evrst 1956 as the datum, followed by masking and cropping of the study area.

(1) Band 1, 2, 3 and 4 of Landsat 1973 data to 79 m.
(2) Band 1, 2, 3 and 4 of Landsat TM of 1992 to 30 m.
(3) Band 1, 2, 3, 4, 5 and 7 of Lansat ETM+ to 30 m.
(4) MODIS bands 1 to 7 to 250 m.
(5) IRS LISS-III band 1, 2 and 3 to 23.5 m.
(6) Thermal band of TM (resampled to 120 m), ETM+ (to 60 m) and MODIS (to 1 km) and Panchromatic bands of ETM+ (resampled to 15 m).

Computation of Shannon's Entropy: The Shannon's entropy (Yeh and Li, 2001) was computed to detect the urban sprawl phenomenon given by equation 1.

$$H_n = -\sum P_i \log_e(P_i) \tag{1}$$

where, P_i is the Proportion of the variable in the ith zone n the total number of zones. This value ranges from 0 to log n, indicating very compact distribution for values closer to 0. The values closer to log n indicates that the distribution is much dispersed. Larger value of entropy reveals the occurrence of urban sprawl.

Principal Component Analysis (PCA): Principal components representing maximum variability of the original datasets were chosen based on eigen values. PCA was carried out to reduce the dimensionality with

i. Bands 1, 2, 3 and 4 of Landsat MSS data.
ii. Band 1, 2, 3 and 4 of Landsat TM.
iii. Band 2, 3, 4, 5 and 7 of Landsat ETM+.
iv. Bands 1 to 7 of MODIS data (of 2002 and 2007).

The purpose of this process is to compress all the information contained in an original m – band data set into fewer than m "new bands" or components. The new components are then used in lieu of the original data and may be applied as a preprocessing procedure prior to automated classification process of the data.

Let m be the total number of bands and n be the number of pixels in each band. To every pixel, we associate a m-dimensional feature vector with components corresponding to the gray values of the m bands. The sample mean of the pixels is defined by

$$\mu = \frac{1}{n}\sum_{i=1}^{n} \mathbf{x}_i \tag{2}$$

where, μ is the mean of the feature vector, x_i is the feature vector of the ith pixel and n is the total number of pixels. The covariance matrix is defined as

$$\sum_x = E\{(x-\mu)(x_n-\mu)^T\} \tag{3}$$

In equation 3, the superscript 'T' denotes vector transpose. An unbiased estimate of the sample covariance matrix **C** is given by

$$C = \frac{1}{n-1}\sum_{i=i}^{n}(x_i-\mu)(x_i-\mu)^T \tag{4}$$

Next, the eigenvalues and eigenvectors of the matrix C are computed by solving

$$(C - \lambda_i \times I) \times e_i = 0 \tag{5}$$

where $e_i = (a_1, a_2, \ldots, a_m)^I$ is the eigenvector corresponding to the eigenvalues λ_i and I is the identity matrix. The eigenvalues λ_i , are determined by solving the characteristic equation

$$| C - \lambda * I | = 0 \tag{6}$$

A new coordinate system is formed by normalized eigenvectors of the covariance (or correlation) matrix C. The mapping of each feature vector $x = (x_1, x_2, x_3 \ldots\ldots x_m)$ on the i^{th} principal component is given by:

$$f_i = \mathbf{x} * e_i = x_1 * e_1^{\,i} + x_2 * e_2^{\,i} + \ldots\ldots + x_m * e_m^{\,i} \tag{7}$$

Chosen Principal Components represents maximum variability of the original datasets.

Fusion: Image fusion is a concept of combining multiple images of different spatial and spectral resolution into composite images with better spatial and spectral resolution. The result of image fusion is a new image which is more suitable for human and machine perception or further image processing tasks such as segmentation, feature extraction and object recognition (Pajares *et al.*, 2004). RGB – HIS algorithm was used to fuse

(1) PC1, PC2 and PC3 of Landsat MSS data (of 1973 with a spatial resolution of 79 m) with PC1 of Landsat TM data (of 1992 with a spatial resolution of 30 m).
(2) Band 2, 3 and 4 of Landsat ETM+ data (of 2000 with a spatial resolution of 30 m) with Landsat ETM+ band 8 (panchromatic data with spatial resolution 15m)

(3) PC1, PC2 and PC3 of MODIS data (of 2002 and 2007 with a spatial resolution of 250 m) with PC1 of Landsat ETM+ data (of 2000 with a spatial resolution of 30 m).

Finally, Landsat MSS, TM, ETM+ and MODIS data were all at 30 m spatial resolution. In GB – HIS algorithm (Carper *et al.*, 1990) the low resolution data are transformed to the IHS (I: intensity, H: hue, S: saturation) color space as equation 8, 9 and 10.

$$\begin{pmatrix} I \\ V_1 \\ V_2 \end{pmatrix} = \begin{pmatrix} \frac{1}{3} & \frac{1}{3} & \frac{1}{3} \\ \frac{1}{\sqrt{6}} & \frac{1}{\sqrt{6}} & -\frac{2}{\sqrt{6}} \\ \frac{1}{\sqrt{2}} & -\frac{1}{\sqrt{2}} & 0 \end{pmatrix} \begin{pmatrix} R \\ G \\ B \end{pmatrix} \tag{8}$$

R, G and B corresponds to PC1, PC2 and PC3 (of Landsat MSS and MODIS) or Band 2, 3 and 4 (of Landsat ETM+)

$$H = \tan^{-1}\left(\frac{V_2}{V_1}\right) \tag{9}$$

$$S = \sqrt{V_1^2 + V_2^2} \tag{10}$$

Here V_1, V_2 are the intermediate variables. I is replaced with high spatial resolution image (like PC1 of Landsat TM for fusing with Landsat MSS; PC1 of ETM+ for fusing with MODIS; and Panchromatic band 8 of Landsat ETM+ to fuse with band 2, 3, and 4 of the same sensor). Then, the fused images of high spatial resolution are obtained by performing an inverse transformation of IHS back to the original RGB as given in equation 11.

$$\begin{pmatrix} R \\ G \\ B \end{pmatrix} = \begin{pmatrix} 1 & \frac{1}{\sqrt{6}} & \frac{1}{\sqrt{2}} \\ 1 & \frac{1}{\sqrt{6}} & -\frac{1}{2} \\ 1 & -\frac{2}{\sqrt{6}} & 0 \end{pmatrix} \begin{pmatrix} I \\ V_1 \\ V_2 \end{pmatrix} \tag{11}$$

Supervised Classification using Bayesian Classifier: In supervised classification, the pixel categorization process is done by specifying the numerical descriptors of the various land cover types present in a scene. It involves three steps –

i. **Training stage:** identifying representative training areas and developing a numerical description of the spectral attributes of each land cover type in the scene, known as *training set*,

ii. **Classification stage:** each pixel in the image data set is categorized into the land cover class it most closely resembles, and

iii. **Output stage:** the process consists of a matrix of interpreted land cover category types.

The following section discusses the classification strategies that use the *training set* descriptions of the category spectral response patterns as interpretation keys by which pixels of unidentified cover types are categorised into their appropriate classes.

Training samples were collected according to the classes given by $D_1,\ldots, Dc$ (built up, vegetation, water bodies and others), where the samples in D_j were i.i.d (independent and identically distributed) random variables with probability $p(x|\omega_k)$ having known parametric form, which could be determined uniquely by the value of a parameter vector Θ_c. Because of dependence of $p(x|\omega_c)$ on Θ_c, $p(x|\omega_c)$ can be written as $p(x|\omega_c, \Theta_c)$. We use the information provided by training data to obtain estimates for unknown parameter vectors $\Theta_1, \Theta_2, , \Theta_c$ Assuming that samples in D_i give no information about Θ_c if $i \neq c$, i:e., parameters for the different classes are functionally independent. So,

$$p(D|\theta)=\prod_{k=1}^{n} p(x_k|\theta) \tag{12}$$

Let Θ denote the p-component vector $\Theta = (\Theta 1, \ldots, \Theta p)^T$ and let $\nabla\theta$ be the gradient operator, so $l(\Theta) \equiv \ln p(D|\Theta)$ that maximizes the log likelihood is $\hat{\theta}=\arg\max l(\theta)$ over Θ.

$$\text{Now } l(\theta) = \sum_{k=1}^{n} \ln p(x_k|\theta) \tag{13}$$

$$\text{and } \nabla_\theta l = \sum_{k=1}^{n} \nabla\theta \ln p(x_k|\theta) \tag{14}$$

Thus the maximum likelihood estimates for Θ is obtained from the set of p equations, $\nabla\theta l = 0$. A solution to Θ could represent a global, local maximum or minimum out of which one represents a true maximum which is confirmed by the calculating the second derivatives.

In our case, μ_k and Σ_k are unknown, so this constitute the components of the parameter vector Θ. Considering the univariate case, with $\Theta_1 = \mu$ and $\Theta_2 = \sigma^2$, the log-likelihood of a single point is

$$\ln p(x_k \mid \theta) = -\frac{1}{2}\ln 2\pi\theta_2 - \frac{1}{2\theta_2}(x_k - \theta_1)^2 \tag{15}$$

and its derivative is

$$\nabla_\theta l = \nabla_\theta \ln p(x_k \mid \theta) = \begin{bmatrix} \frac{1}{\theta_2}(x_k - \theta_1)^2 \\ -\frac{1}{2\theta_2} + \frac{(x_k - \theta_1)^2}{2\theta_2^2} \end{bmatrix} \tag{16}$$

Applying the full log-likelihood and rearranging the terms, the maximum-likelihood estimate for multivariate case on substituting the $\hat{\mu} = \hat{\theta}_1$ and $\hat{\sigma}^2 = \hat{\theta}_2$ is

$$\hat{\mu} = \frac{1}{n}\sum_{k=1}^{n} x_k \tag{17}$$

$$\hat{\Sigma} = \frac{1}{n}\sum_{k=1}^{n}(x_k - \mu')(x_k - \mu')^T \tag{18}$$

The sample mean and covariance are taken as the maximum-likelihood estimate for the true mean vector and covariance matrix. The covariance matrices are assumed to be different for each category. So the maximum-likelihood quadratic discriminant analysis classifier is

$$g_i(x) = x^T W_i x + w_i^T x + \omega_{io} \tag{19}$$

where

$$W_i = -\frac{1}{2}\sum_i^{-1} \tag{20}$$

$$w_i = -\frac{1}{2}\sum_i^{-1}\mu_i \tag{21}$$

$$\omega_{i0} = -\frac{1}{2}\mu_i^t \sum_i^{-1}\mu_i - \frac{1}{2}\ln|\sum_i| + \ln P(\omega_i) \tag{22}$$

The values of mean $\hat{\mu}$, covariance $\hat{\Sigma}$ and prior probability $P(\omega_i)$ are substituted in the discriminant function as given by equation 19. A pixel is assigned to a particular class for which it has the maximum probability. This provided the supervised classified image from which the *c* classes are obtained.

Accuracy assessment: Accuracy assessments were done with field knowledge, visual interpretation and also referring Google Earth (http://earth.google.com).

Computation of Normalised Difference Vegetation Index (NDVI): Vegetated areas have a relatively high Near-IR (Infrared) reflectance and low visible reflectance. Due to this property of the vegetation, various mathematical combinations of the NIR and the Red band have been found to be sensitive indicators of the presence and condition of green vegetation. NDVI is computed using Equation 23:

$$\frac{NIR - RED}{NIR + RED} \tag{23}$$

It separates green vegetation from its background soil brightness and retains the ability to minimize topographic effects while producing a measurement scale ranging from –1 to +1 with NDVI < 0 representing no vegetation. NDVI is sensitive to the presence of vegetation, since green vegetation usually decreases the signal in the red due to chlorophyll absorption and increases the signal in the NIR wavelength due to light scattering by leaves.

The potential of computing NDVI has created great interest to study global biosphere dynamics. It is preferred to the simple index for global vegetation monitoring because NDVI helps compensate for changing illumination conditions, surface slope, aspect and other extraneous factors. Numerous investigators have related the NDVI to several vegetation phenomena. These phenomena have ranged from vegetation seasonal dynamics at global and continental scales, to tropical forest clearance, leaf area index measurement, biomass estimation, percentage ground cover determination and FPAR (fraction of absorbed photosynthetically active radiation).

Derivation of Land Surface Temperature (LST)

LST from Landsat TM

The TIR band 6 of Landsat-5 TM was used in order to calculate the surface temperature of the area. The digital number (DN) was first converted into radiance L_{TM} using

$$L_{TM} = 0.124 + 0.00563 * DN \tag{Equation 24}$$

The radiance was converted to equivalent blackbody temperature $T_{TMSurface}$ at the satellite using

$$T_{TMSurface} = K_2/(K_1 - \ln L_{TM}) - 273 \tag{Equation 25}$$

The coefficients K_1 and K_2 depend on the range of blackbody temperatures. In the blackbody temperature range 260-300K the default values (Singh, S. M., 1988) for Landsat TM are K_1 = 4.127 and K_2 = 1274.7.

Brightness temperature is the temperature that a blackbody would obtain in order to produce the same radiance at the same wavelength (λ = 11.5 μm). Therefore, additional correction for spectral emissivity (ε) is required to account for the non-uniform emissivity of the land surface. Spectral emissivity for all objects are very close to 1, yet for more accurate temperature derivation emissivity of each land cover class is considered separately. Emissivity correction is carried out using surface emissivities for the specified land covers (table 2) derived from the methodology described in Snyder *et al.*, (1998) and Stathopoulou *et al.* (2006).

Table 2. Surface emissivity values by land cover type

Land cover type	Emissivity
Densely urban	0.946
Mixed urban (Medium Built)	0.964
Vegetation	0.985
Water body	0.990
Others	0.950

The procedure involves combining surface emissivity maps obtained from the Normalized Difference Vegetation Index Thresholds Method ($NDVI^{THM}$) (Sobrino and Raissouni, 2000) with land cover information. The emmissivity corrected land surface temperature (Ts) were finally computed as follows (Artis and Carnhan, 1982)

$$T_s = \frac{T_B}{1+(\lambda \times T_B / \rho)\ln \varepsilon} \qquad \text{(Equation 26)}$$

where, λ is the wavelength of emitted radiance for which the peak response and the average of the limiting wavelengths (λ = 11.5 μm) (Markham and Barker, 1985) were used, ρ = h x c/σ (1.438 x 10^{-2} mK), σ = Stefan Bolzmann's constant (5.67 x 10^{-8} $Wm^{-2}K^{-4}$ = 1.38 x 10^{-23} J/K), h = Planck's constant (6.626 x 10^{-34} Jsec), c = velocity of light (2.998 x 10^8 m/sec), and ε is spectral emissivity.

LST from Landsat ETM+

The TIR image (band 6) was converted to a surface temperature map according to the following procedure (Weng *et al*, 2004). The DN of Landsat ETM+ was first converted into spectral radiance L_{EIM} using equation 27, and then converted to at-satellite brightness temperature (i.e., black body temperature, $T_{ETMSurface}$), under the assumption of uniform emissivity ($\varepsilon \approx 1$) using equation 28 (Landsat Project Science Office, 2002):

$$L_{EIM} = 0.0370588 \text{ x } DN + 3.2 \qquad \text{(Equation 27)}$$

$$T_{ETMSurface} = K2/\ln (K_1/ L_{ETM} + 1) \quad \text{(Equation 28)}$$

where, $T_{ETMSurface}$ is the effective at-satellite temperature in Kelvin, L_{ETM} is spectral radiance in watts/(meters squared x ster x μm); and K_1 and K_2 are pre-launch calibration constants. For Landsat-7 ETM+, K_2 = 1282.71K, K_1 = 666.09 $mWcm^{-2}sr\text{-}1\mu m^{-1}$ were used (http://ltpwww.gsfc.nasa.gov/IAS/handbook/handbook_htmls/chapter11/ chapter11.html). The emissivity corrected land surface temperatures Ts were finally computed by equation 26.

Linear Spectral Unmixing

Linear unmixing is used for solving the mixed pixel problem in the case of coarse resolution data. The hypothesis underlying linear unmixing is that the spectral radiance measured by the sensor consists of the radiances reflected by all of these materials, summed in proportion to the sub-pixel area covered by each material. To the degree that, this hypothesis is valid, and that the endmembers (pure pixels or pixels having only one category) are given by the reference spectra of each of the individual pure materials, and under the condition that these spectra are linearly independent, then in theory one can deduce the makeup of the target pixel by calculating the particular combination of the endmember spectra required to synthesize the target pixel spectrum. A brief outline of the method is mentioned below:

Linear spectral unmixing assumes that the spectrum measured by a sensor is a linear combination of the spectra of all components within the pixel. Therefore,

$$a_{11}x_1 + a_{12}x_2 + a_{13}x_3 \ldots + a_{1j}x_j + \ldots + a_{1n}x_n + e_1 = y_1$$

$$a_{21}x_1 + a_{22}x_2 + a_{23}x_3 \ldots + a_{2j}x_j + \ldots + a_{2n}x_n + e_2 = y_2$$

$$a_{i1}x_1 + a_{i2}x_2 + a_{i3}x_3 \ldots + a_{ij}x_j + \ldots + a_{in}x_n + e_i = y_i$$

$$a_{m1}x_1 + a_{m2}x_2 + a_{m3}x_3 \ldots + a_{mj}x_j + \ldots + a_{mn}x_n + e_m = y_m$$

where,

- m = Nmber of bands in the multispectral data set
- n = Number of distinct classes of objects.
- $y_{1, 2, \ldots, m}$ = Spectral reflectance of the pixel in 1_{st}, 2_{nd}, 3_{rd}, ..., m_{th} spectral band of a pixel contain one or more components
- a_{ij} = Spectral reflectance of the *jth* component in the pixel for ith spectral band.
- x_j = Proportion value of the *jth* component in the pixel
- e_i = Error term for the *ith* spectral band
- j = 1, 2, 3 ... n (Number of components assumed)
- i = 1, 2, 3 ... m (Number of Spectral bands for the sensor system)

The error term (e_i) is due to the assumption made that the response of each pixel in any spectral wavelength is a linear combination of the proportional responses of each component. The above equations can also be written as:

$$y_i = \sum_{j=1}^{n} (a_{ij} x_{ij}) + e_i$$

or, AX=Y, assuming that the error term is 0.
Then, AX-Y$\approx$ 0 (if $e_1, e_2, \ldots, e_i, \ldots, e_m = 0$)
where, A is a m x n matrix ($a_{11}, a_{12}, \ldots, a_{mn}$), X is a n x 1 vector ($x_1, x_2, \ldots, x_n$) and Y is a n x 1 vector ($y_1, y_2, \ldots, y_n$). Therefore, the above set of equations can be written as,

$$\begin{bmatrix} a_{11} & a_{12} & \ldots & a_{1n} \\ a_{21} & a_{22} & \ldots & a_{2n} \\ \vdots & \vdots & \vdots & \vdots \\ a_{m1} & a_{m2} & \ldots & a_{mn} \end{bmatrix} \begin{bmatrix} x_1 \\ x_2 \\ \vdots \\ x_n \end{bmatrix} = \begin{bmatrix} y_1 \\ y_2 \\ \vdots \\ y_n \end{bmatrix}$$

If m < n, many solutions exist; if m = n and A is invertible (full rank matrix), a solution exist and it is unique; if m > n, (a) solution may not exist (b) a unique solution exists. The solution of x is obtained by minimizing the function $\|AX - Y\|$. Various solutions can be obtained when $\|AX - Y\|$ is minimized with different constraints on x.

Unconstrained Case

$x_1+x_2+\ldots+x_n \neq 1$, where x is any arbitrary real number. Now our aim is to minimize the difference between AX and Y so that the error term is zero. Since A, X and Y are vectors, so the difference (length) or norm of these vectors can be given by

$$\|AX - Y\|^2$$

$$= (AX - Y)^T (AX - Y)$$

$$= ((AX)^T - Y^T)(AX - Y)$$

$$= A^T X^T AX - X^T A^T Y - Y^T AX + Y^T Y \qquad \text{(Equation 29)}$$

Considering the 3rd term $Y^T AX$, let AX=Z, $Y^T AX = Y^T Z = Z^T Y$.
Therefore, $Y^T AX = (AX)^T Y = X^T A^T Y$. Now, equation 29 can be written as

$$= A^T X^T AX - X^T A^T Y - X^T A^T Y + Y^T Y$$

$$= A^T X^T AX + Y^T Y - 2X^T A^T Y$$

Assume $J = A^T X^T AX + Y^T Y - 2X^T A^T Y$

Differentiating w.r.t X

$$\frac{\partial J}{\partial X} = 2A^T AX - 2A^T Y = 0$$

$A^T AX = A^T Y$

$$X_{unconstrained} = (A^T A)^{-1} A^T Y \qquad \text{(Equation 30)}$$

which is termed as the Unconstrained Least Squares (ULS) estimate of the abundance. The negative abundance values can be considered to be zero and the values exceeding one can be considered to be 1.

Constrained Case

Imposing the sum-to-one constraint on the abundance values i.e. $x_1+x_2+\ldots+x_n = 1$ or $\sum_{i=1}^{n} x_i = 1$.

The solution to the above problem can be solved by minimizing the function

$J(X, \lambda) = AX - Y + \lambda (1^T X - 1)$

where λ is the Lanrangian multiplier. The purpose of introducing the Lanrangian multiplier is to convert the constrained case to the unconstrained case for which we have the above solution.

Proceeding as earlier,

$\|AX - Y\|^2 + \lambda (1^T X - 1)$

$= (AX - Y)^T (AX - Y) + \lambda (1^T X - 1)$

$= ((AX)^T - Y^T) (AX - Y) + \lambda (1^T X - 1)$

$= A^T X^T AX - X^T A^T Y - Y^T AX + Y^T Y + \lambda (1^T X - 1)$

$= A^T X^T AX + Y^T Y - 2X^T A^T Y + \lambda (1^T X - 1)$

Differentiating $J(X, \lambda)$ w.r.t. X

$$\frac{\partial J}{\partial X} = 2A^T AX - 2A^T Y - \lambda 1 = 0 \qquad \text{(Equation 31)}$$

Differentiating J(X, λ) w.r.t. λ

$$\frac{\partial J}{\partial \lambda} = X^T 1 - 1 = 0 \text{ or, } X^T 1 = 1$$

Now, from equation 9, $2A^T AX = 2A^T Y - \lambda 1$

$$\text{or, } A^T AX = A^T Y - (\frac{\lambda}{2})1$$

$$\text{or, } X = (A^T A)^{-1}(A^T Y - (\frac{\lambda}{2})1)$$

$$\text{or, } X_{constrained} = (A^T A)^{-1} A^T Y - \frac{\lambda}{2}(A^T A)^{-1} 1 \qquad \text{(Equation 32)}$$

Multiplying both sides by 1^T,

$$\text{or, } 1^T X = 1^T (A^T A)^{-1} A^T Y - \frac{\lambda}{2} 1^T (A^T A)^{-1} 1$$

$$\text{therefore, } \lambda = -\frac{2(1^T X - 1^T (A^T A)^{-1} A^T Y}{1^T (A^T A)^{-1} 1}$$

$$\text{so, } \lambda = -\frac{2(1 - 1^T (A^T A)^{-1} A^T Y}{1^T (A^T A)^{-1} 1} \text{ (since } 1^T X = 1) \qquad \text{(Equation 33)}$$

Equation 33 can also be written as $\lambda = -\frac{2(1 - 1^T X_{unconstrained})}{1^T (A^T A)^{-1} 1}$

Substituting the value of λ from equation (33) in equation (32), we get,

$$X_{constrained} = (A^T A)^{-1} A^T Y + \frac{2(1 - 1^T ((A^T A)^{-1} A^T Y))}{2(1^T (A^T A)^{-1})} (A^T A)^{-1} 1$$

$$X_{constrained} = (A^T A)^{-1} A^T Y + \frac{(1 - 1^T((A^T A)^{-1} A^T Y))}{1^T (A^T A)^{-1}} (A^T A)^{-1} 1 \quad \text{(Equation 34)}$$

Equation 34 gives the Constrained Least Squares (CLS) estimate of the abundance.

Catchment Yield and Land Use

Flows at the catchment were indirectly estimated by the land use area, runoff coefficient and precipitation. Land use is the use of land by humans, usually with emphasis on the functional role of land such as land under buildings, plantation, pastures, etc. Land use pattern in the catchment has direct implications on hydrological yield. The yield of a catchment area is the net quantity of water available for storage, after all losses, for the purpose of water resource utilization and planning (Ramachandra *et al.* 1999). Runoff is the balance of rainwater, which flows or runs over the natural ground surface after losses by evaporation, interception and infiltration. The runoff from rainfall was estimated by rational method that is used to obtain the yield of a catchment area by assuming a suitable runoff coefficient.

$$\text{Yield} = C \times A \times P \quad (35)$$

where, C: runoff coefficient, A: catchment area and P: rainfall.

The value of C varies depending on the soil type, vegetation, geology, etc. from 0.1 to 0.2 (heavy forest), 0.2 to 0.3 (sandy soil), 0.3 to 0.4 (cultivated absorbent soil), 0.4 to 0.6 (cultivated or covered with vegetation), 0.6 to 0.8 (slightly permeable, bare) to 0.8 to 1.0 (rocky and impermeable).

Results and Discussion

Shannon's entropy computed for Bangalore city, Peri-urban and outskirts (hence n = 3), together comprising Greater Bangalore for 1973, 1992, 2000 and 2006 are listed in Table 3. The entropy values obtained for 2000 and 2006, (1.0325 and 1.0782) are closer to the upper limit of log *n*, i.e. 1.0986, showing the higher degree of dispersion of built-up in the city. The urbanisation process increased in 2000 and 2006, indicating higher entropy value as the distribution of built-up during 2006 was more dispersed than in 1973 or 1992.

Table 3. Shannon's entropy for Greater Bangalore

Year→	**1973**	**1992**	**2000**	**2006**
Entropy	0.9007	0.9023	1.0325	1.0782
ln(n)	1.0986			

Supervised classification was performed using Bayesian classifier and was verified with field knowledge, visual interpretation and Google Earth image. The supervised classified images of 1973, 1992, 1999, 2000, 2002, 2006 and 2007 with an overall accuracy of 72%, 75%, 71%, 77%, 60%, 73% and 55% were obtained by using the open source programs (i.gensig, i.class and i.maxlik) of Geographic Resources Analysis Support System (http://wgbis.ces.iisc.ernet.in/ grass) as displayed in Figure 4. The class statistics is given in table 4. The implementation of the classifier on Landsat, IRS and MODIS image helped in the digital data exploratory analysis as were also verified from field visits in July, 2007 and Google Earth image.

Table 4. Greater Bangalore land cover statistics

Class → Year ↓		Built up	Vegetation	Water Bodies	Others
1973	Ha	5448	46639	2324	13903
	%	7.97	68.27	3.40	20.35
1992	Ha	18650	31579	1790	16303
	%	27.30	46.22	2.60	23.86
1999	Ha	23532	31421	1574	11794
	%	34.44	45.99	2.30	17.26
2000	Ha	24163	31272	1542	11346
	%	35.37	45.77	2.26	16.61
2002	Ha	26992	28959	1218	11153
	%	39.51	42.39	1.80	16.32
2006	Ha	29535	19696	1073	18017
	%	43.23	28.83	1.57	26.37
2007	Ha	30876	17298	1005	19143
	%	45.19	25.32	1.47	28.01

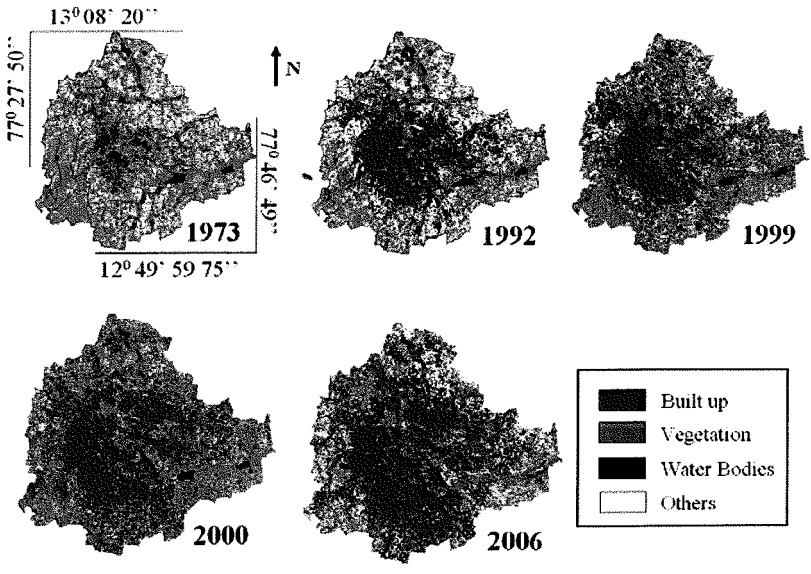

Figure 4. Temporal land use changes in Greater Bangalore

From the classified raster data, urban class was extracted and converted to vector representation for computation of precise area in hectares. There has been a 466% increase in built up area from 1973 to 2007 as evident from temporal analysis leading to a sharp decline of 61% area in water bodies in Greater Bangalore mostly attributing to intense urbanisation process. Figure 5 shows Greater Bangalore with 265 water bodies (in 1972). The rapid development of urban sprawl has many potentially detrimental effects including the loss of valuable agricultural and eco-sensitive (e.g. wetlands, forests) lands, enhanced energy consumption and greenhouse gas emissions from increasing private vehicle use. Vegetation has decreased by 32% from 1973 to 1992, by 38% from 1992 to 2002 and by 63% from 2002 to 2007.

Disappearance of water bodies or sharp decline in the number of waterbodies in Bangalore is mainly due to intense urbanisation and urban sprawl. Many lakes were unauthorisedly encroached for illegal buildings (54%). Field survey (during July-August 2007) shows that nearly 66% of lakes are sewage fed, 14% surrounded by slums and 72% showed loss of catchment area. Also, lake catchments were used as dumping yards for either municipal solid waste or building debris. The surrounding of these lakes have illegal constructions of buildings and most of the times, slum dwellers occupy the adjoining areas. At many sites, water is used for washing and household activities and even fishing was observed at one of these sites. Multi-storied buildings have come up on some lake beds that have totally intervene the natural catchment flow leading to sharp decline and deteriorating quality of waterbodies.

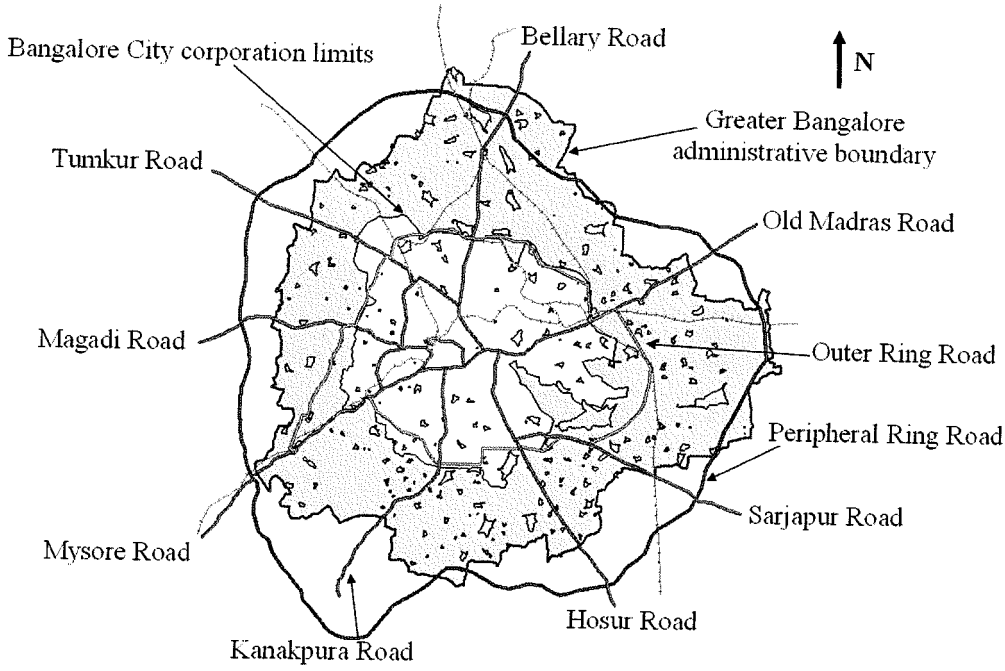

Figure 5. Greater Bangalore with 265 water bodies.

Urbanisation has telling influences on the natural resources evident from the sharp decline in number of water bodies and also from depleing groundwater table. Temporal analyses indicate the decline of 34.48% during 1973 to 1992, 56.90% during 1973-2002 and 70.69% of waterbodies during 1973-2007 in the erstwhile Bangalore city limits. Similar analyses done for Greater Bangalore (i.e Bangalore city with surrounding 8 municipalities) indicate the decline of 32.47% during 1973 to 1992, 53.76% during 1973-2002 and 60.83% during 1973-2007 (Table 5). This is correlated with the increase in built up area from the concentrated growth model focusing on Bangalore, adopted by the state machinery, affecting severely open spaces and in particular waterbodies. Some of the lakes have been restored by the city corporation and the concerned authorities in recent times. Figure 1, given earlier shows the rate of increase in built up from 1973 to 2007 and its implication on the decline of vegetation and water bodies.

Table 5. Status of water bodies in Bangalore city limits and Greater Bangalore

	Bangalore City		Greater Bangalore	
	Number of Water bodies	Area (in ha)	Number of Water bodies	Area (in ha)
SOI	58	406	207	2342
1973	51	321	159	2003
1992	38	207	147	1582
2002	25	135	107	1083
2007	17	87	93	918

The land cover features that have been classified using the ML estimates and Bayesian theory shows that builtup and vegetation are negatively correlated given by:

$$y = -8E\text{-}06x^2 - 0.7362x + 50472,\ R^2 = 0.9286 \tag{36}$$

where, y is the independent variable (builtup) and x is the dependent variable (vegetation). Builtup and water bodies are also negatively correlated as given by:

$$y = -8E\text{-}07x^2 - 0.0148x + 2111.9,\ R^2 = 0.9953 \tag{37}$$

where, y is builtup (independent) and x is water bodies (dependent). Table 5 gives the details of the number of wetlands from 1973 to 2007.

Pattern classifiers were used to map waterbodies automatically from NIR bands of MODIS and Landsat remote sensing data. MODIS provided data of 2002 to 2007, while for 1973 and 1992, IR Bands of Landsat (79m and 30m spatial resolution) data were used. Principal Components of IR bands of MODIS (250 m) were fused with IRS LISS-3 NIR (23.5 m). To extract waterbodies, statistical unsupervised learning of IR bands for the respective temporal data was performed using Bayesian approach based on prior probability, mean and covariance. Spatial distribution of waterbodies on temporal scale is given in Figure 6. Temporal analysis of waterbodies indicate sharp decline of 58% in Greater Bangalore attributing to intense urbanisation process, evident from 466% increase in builtup area from 1973 to 2007.

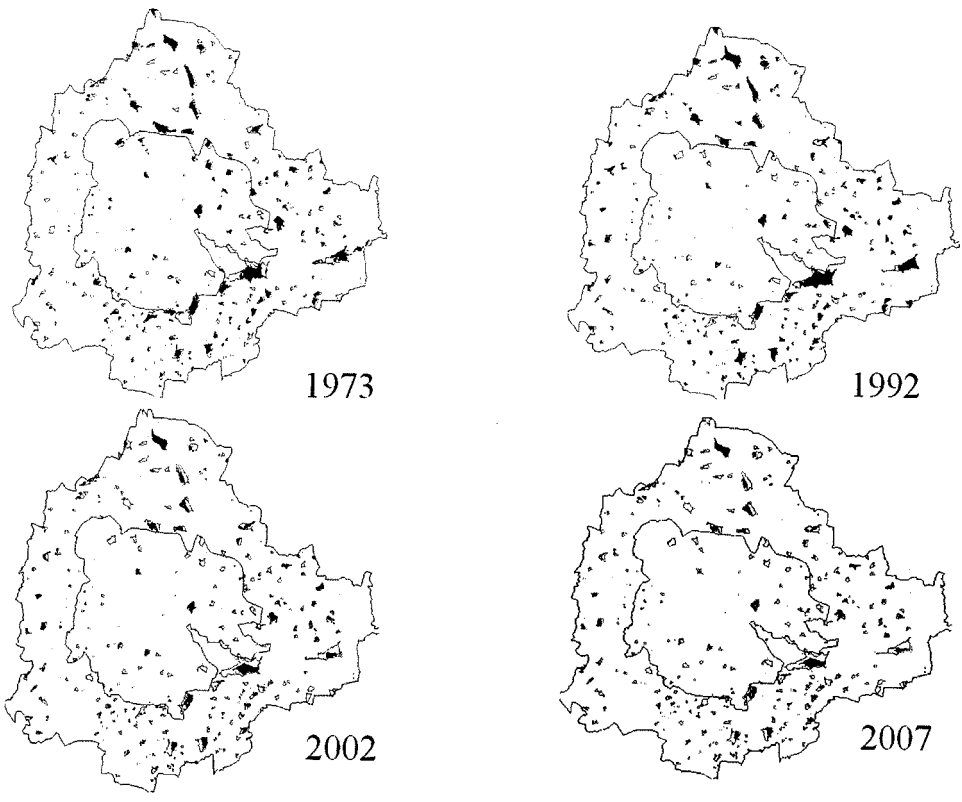

Figure 6. Spatio-temporal analysis of wetlands of Greater Bangalore. Water bodies are represented in blue and the vector layer of water bodies generated from SOI Toposheet is overlaid in red. The inner boundary (in black) is the Bangalore city limits and the outer boundary represents the spatial extent of Greater Bangalore.

Urbanisation and the consequent loss of lakes has led to decrease in catchment yield, water storage capacity, wetland area, number of migratory birds, flora and fauna diversity and ground water table. Studies in selected lake catchments in Bangalore reveal the decrease in depth of the ground water table from 10-12 m to 100-200 m in 20 years due to the disappearance of wetlands.

Reclamation of lakes for various developmental activities has resulted in the loss of interconnectivity in Bangalore district leading to higher instances of floods even during the normal rainfall. Analyses of Bellandur and Ulsoor drainage network (Fig. 7) showed that the network is lost due to conversion of Chelgatta tank into a golf course. Similarly the drainage network between Madivala and Bellandur revealed of encroachment and conversion that has resulted in the loss of connectivity between Yelchenhalli kere and Madivala (Fig. 8).

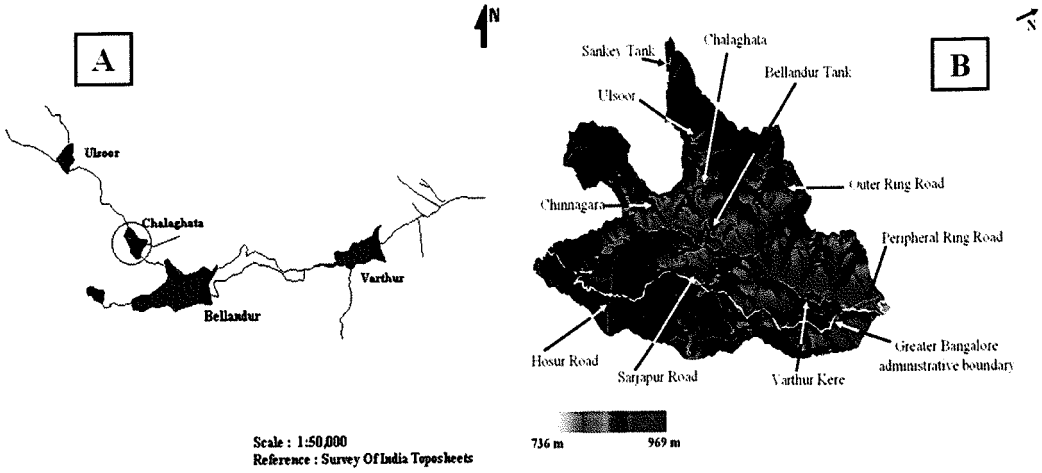

Figure 7. Ulsoor–Bellandur–Varthur (a) drainage network (b) lakes overlaid on 10 m DEM showing their missing interconnectivity

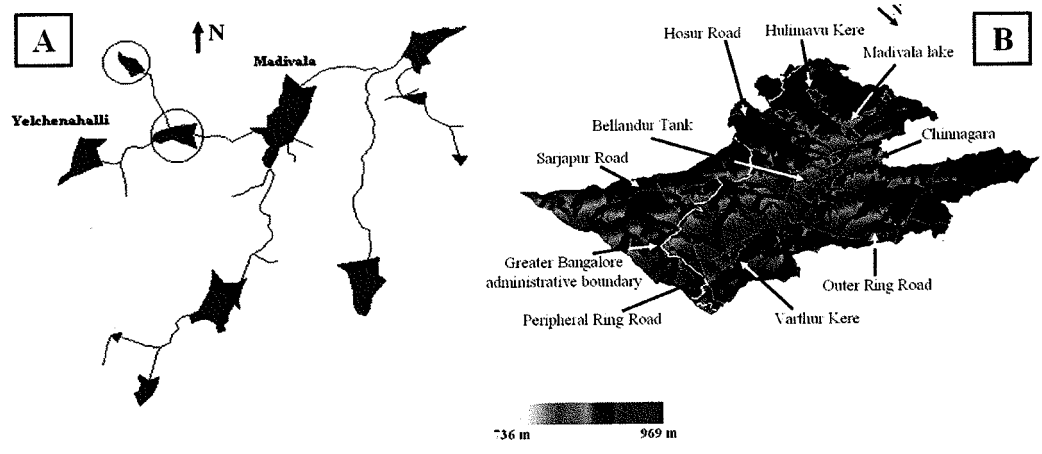

Figure 8. Madivala–Bellandur–Varthur (a) drainage network (b) lakes overlaid on 10 m DEM showing their missing interconnectivity

Increased peak discharge and higher frequency of floods are the consequences of urbanisation. As land is converted from fields to built up, it loses its ability to absorb rainfall. Urbanisation has increased runoff 2 to 6 times over what would occur on natural terrain in some pockets of Bangalore. During periods of urban flooding, streets become swift moving rivers, while low lying residential areas and basements become death traps as they fill with water. Conversion of water bodies to residential layouts has further exaggerated the problem.

Flooding in urban areas causes large damage at buildings and other public and private infrastructure (evident during 1997, 2002 and 2007). Besides, street flooding can limit or completely hinder the functioning of traffic systems and has indirect consequences such as

loss of business and opportunity. The expected total damage; direct and indirect monetary damage costs as well as possible social consequences is related to the physical properties of the flood, i.e. the water level above ground level, the extent of flooding in terms of water volume escaping from or not being entering the drainage system, and the duration of flooding.

Ulsoor–Belandur catchment: This catchment has 6 lakes – Sankey, Ulsoor, Chalghata, Chinnagara and Varthur and was classified into three major land use types – built up, vegetation and others (comprising open land, waste land etc). The total rainfall yield in this catchment is 240 Mm^3, percolated water is 90 Mm^3 and water overflow is 150 Mm^3. The SRTM DEM data were resampled to 10 m resolution and the volume of each lake was computed assuming the depth to be 1 m and the mean annual rainfall to be 850 mm. The total volume of all the 6 lakes in this catchment is 73 Mm^3. Hence there is surplus overland flow of 77 Mm^3, which cannot flow to downstream due to disruption of natural drainage (removal of lakes and blockage of storm water drains) resulting in flooding (even during normal rainfall).

Madivala–Varthur catchment: Similar analysis was done for Madivala catchment which has 14 lakes – Venkatapura, Yellakunte, Bandepalya, Begur Doddakere, Madivala, Hulimavu, Marenahalli, Govindanaikana kere, Tank north of Doresanipalya, Gittigere and Vaddarpalya. The total rainfall yield is 247 Mm^3, percolated water is 97 Mm^3 and the remaining 150 Mm^3 water flows as overland flow and storage in lakes. The total volumes of all the lakes considering 1 m depth is 110 Mm^3 resulting in the excess of 40 Mm^3 from the catchment leading to artificial floods. In addition to rainfall, Belandur-Varthur watershed receives untreated municipal sewage to the order of 500MLD.

Landsat ETM+ data of 15 m spatial resolution (on fusing with Landsat ETM+ PAN) have been used to estimate impermeable areas that does not distinguish between types of urban land use (industrial, commercial and residential) but consist of a sample from a mixture of residential and commercial areas. Figure 9 shows the relation found between impermeable area to urban population density. Consequence of increase in built up pixels (evident from the increase in paved surface or impermeable area) is the increase of population density in a region. Also, due to increased paved surface and concentrated human activities the magnitude of the difference in observed ambient air temperature between urban pockets (artificial land surface) and the regions covered with vegetation (natural area), which is ascribed as urban heat island effect. The urban heat-island effect results in increased local atmospheric and surface temperatures in urban pockets compared to the surrounding open spaces, etc. Specifically, surface and atmospheric temperatures are increased by anthropogenic heat discharge due to energy consumption, increased land surface coverage by artificial materials having high heat capacities and conductivities, increased vehicular and industrial emissions and the associated decreases in vegetation and water pervious surfaces, which reduce surface temperature through evapotranspiration. An attempt is made here to understand the implications of land cover changes on local climate.

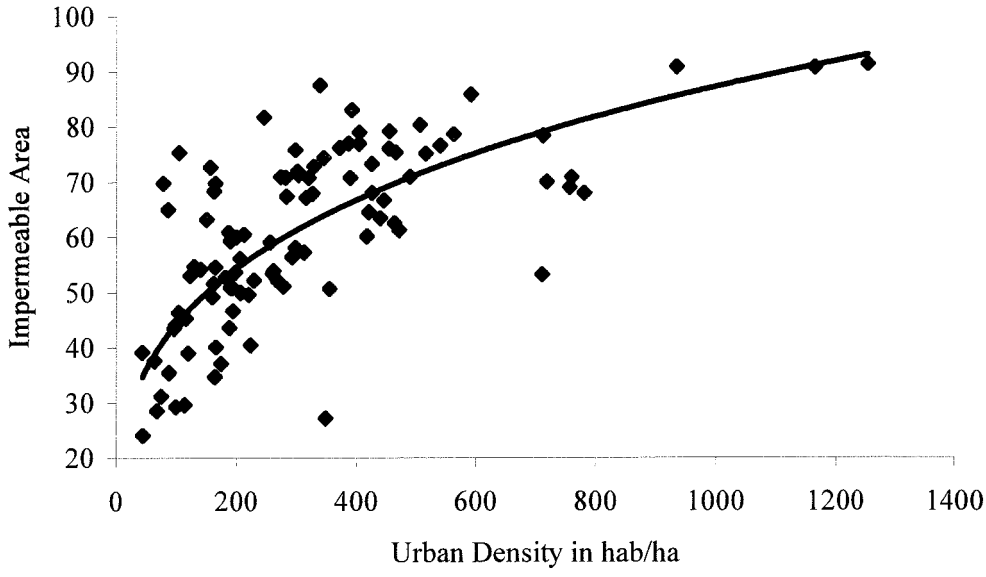

Figure 9. Impermeable area and urban density for Bangalore city

Computation of LSTfrom Landsat TM/ETM+ and MODIS Thermal Bands

LST were computed from Landsat TM and ETM thermal bands. The minimum and maximum temperatures from Landsat TM data of 1992 were 12 and 21 with a mean of 16.5±2.5 while for ETM+ data were 13.49 and 26.32 with a mean of 21.75±2.3. MODIS Land Surface Temperature/Emissivity (LST/E) data with 1 km spatial resolution with a data type of 16-bit unsigned integer were multiplied by a scale factor of 0.02 (http://lpdaac.usgs.gov/modis/dataproducts.asp#mod11). The corresponding temperatures for all data were converted to degree Celsius. Figure 10 shows the LST map and NDVI of Greater Bangalore in 1992, 2000 and 2007. The minimum and maximum temperatures were computed as 20.23, 28.29 and 23.79, 34.29 with a mean of 23.71±1.26, 28.86±1.60 for 2000 and 2007 respectively. Data were calibrated with in-situ measurements.

Computation of NDVI from Landsat TM/ETM+ and MODIS Data

NDVI was computed from visible Red (0.0.63 – 0.69 μm) and NIR (0.76 – 0.90 μm) bands of Landsat TM (1992)/ETM+ (2000) and MODIS data (620 – 670 μm (Red) and 841 – 876 μm (NIR)) of 2007, so that the relationship between LST and NDVI can be studied (Fig. 10). NDVI for Landsat TM was 0.04±0.4543, for ETM+ was 0.0252±0.5369 and for MODIS was -0.0917±0.5131.

The correlation between NDVI and temperature of 1992 TM data was 0.88, 0.72 for MODIS 2000 and 0.65 for MODIS 2007 data respectively, suggesting that the extent of land

cover with vegetation plays a significant role in the regional LST. Respective NDVI and LST for different land uses is given in table 6 and further analysis was carried out to understand the role of respective land uses in the regional LST's. Temporal analysis showed a linear growth of 466% in number of urban pixels from 1973 to 2007 and a decline of 61% in the number of water bodies with a 63% decrease in vegetation cover. Similarly during 1992 to 2007, the increase in built pixels was 63% while vegetation and water bodies declined by 45 and 43.8% respectively. The increase in LST during 2002 and 2007 compared to 1992 could be mainly attributed to the increase in built up area and decline of area under vegetation and water bodies in the region

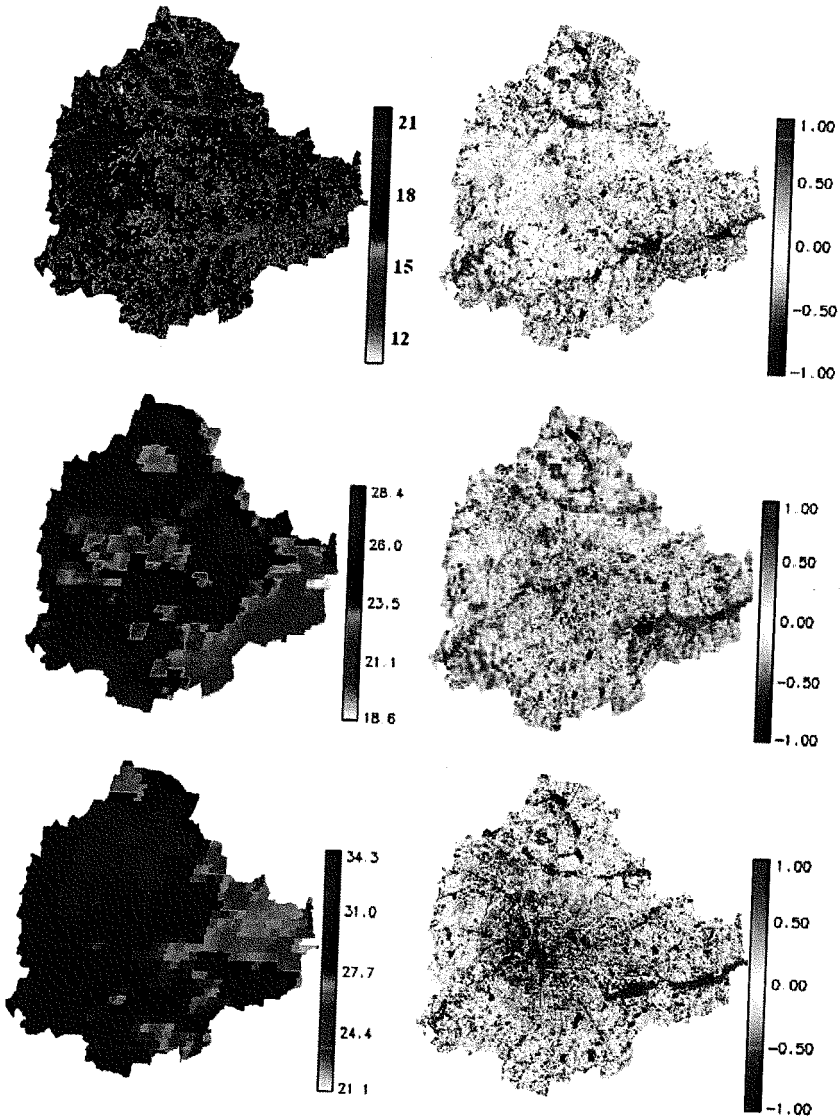

Figure 10. LST and NDVI from Landsat TM (1992), MODIS (2002 and 2007)

(Note: pixelisation of MODIS 2002 and 2007 is mainly due to coarse spatial resolution ~ 1 Km)

Table 6. LST (°C) and NDVI for various land uses

Land use	1992 (TM)		2000 (MODIS)		2007 (MODIS)	
	LST Mean±SD	NDVI Mean±SD	LST Mean±SD	NDVI Mean±SD	LST Mean±SD	NDVI Mean±SD
Built up	19.03± 1.47	-0.162± 0.096	26.57± 1.25	-0.614± 0.359	31.24± 2.21	-0.607± 0.261
Vegetation	15.51± 1.05	0.467± 0.201	22.21± 1.49	0.626± 0.27	25.79± 0.44	0.348± 0.42
Water bodies	12.82± 0.62	-0.954± 0.055	21.27± 1.03	-0.881± 0.045	24.20± 0.27	-0. 81± 0.27
Open ground	17.66± 2.46	-0.106± 0.281	24.73± 1.56	-0.016± 0.283	28.85± 1.54	-0.097± 0.18

It is clear that urban areas that include commercial, industrial and residential land exhibited the highest temperature followed by open ground. Lowest temperatures were observed in water bodies across all years and vegetation. Spatial variation of NDVI is not only subject to the influence of vegetation amount, but also to topography, slope, solar radiation availability, and other factors (Walsh *et al.*, 1997). A closer look at the values of NDVI by land use category (table 6) indicates that the relationship between LST and NDVI may not be linear. Clearly, it is necessary to further examine the existing LST and vegetation abundance relationship using fraction as an indicator, which is discussed next.

Generation of Abundance Maps Through Linear Spectral Unmixng

The Landsat ETM+ images (band 1, 2, 3, 4, 5 and 7) were unmixed through Linear unmixing to get the abundance maps of 5 classes (1) dense urban (commercial/industrial/residential), (2) mixed urban (that has some amount of vegetation present in between), (3) vegetation, (4) open ground and (5) water bodies. We considered only dense urban, mixed urban and vegetation abundance for further analysis as shown in Figure 11. Minimum and maximum temperature from ETM+ data were 13.49 and 26.32 with a mean of 21.75±2.3.

These abundance images were further analysed to see their contribution to the UHI by separating the pixels that contains 0-20%, 20-40%, 40-60%, 60-80% and 80-100% of urban pixels. Table 7 gives the average LST for various land cover (LC) abundance classes.

Table 7. Mean LST for various Land use classes with varying abundances

Class → Abundance ↓	Mean Temperature ± SD of dense urban	Mean Temperature ± SD of mixed urban	Mean Temperature ± SD of vegetation
0-20%	21.99±2.37	21.57±2.36	17.91±2.19
20-40%	22.06±2.15	21.58±2.36	17.39±1.37
40-60%	22.27±2.00	21.67±2.41	17.22±0.89
60-80%	22.33 ±2.22	22.28±2.02	17.13±0.85
80-100%	22.47±1.96	22.37±2.17	17.12±0.91

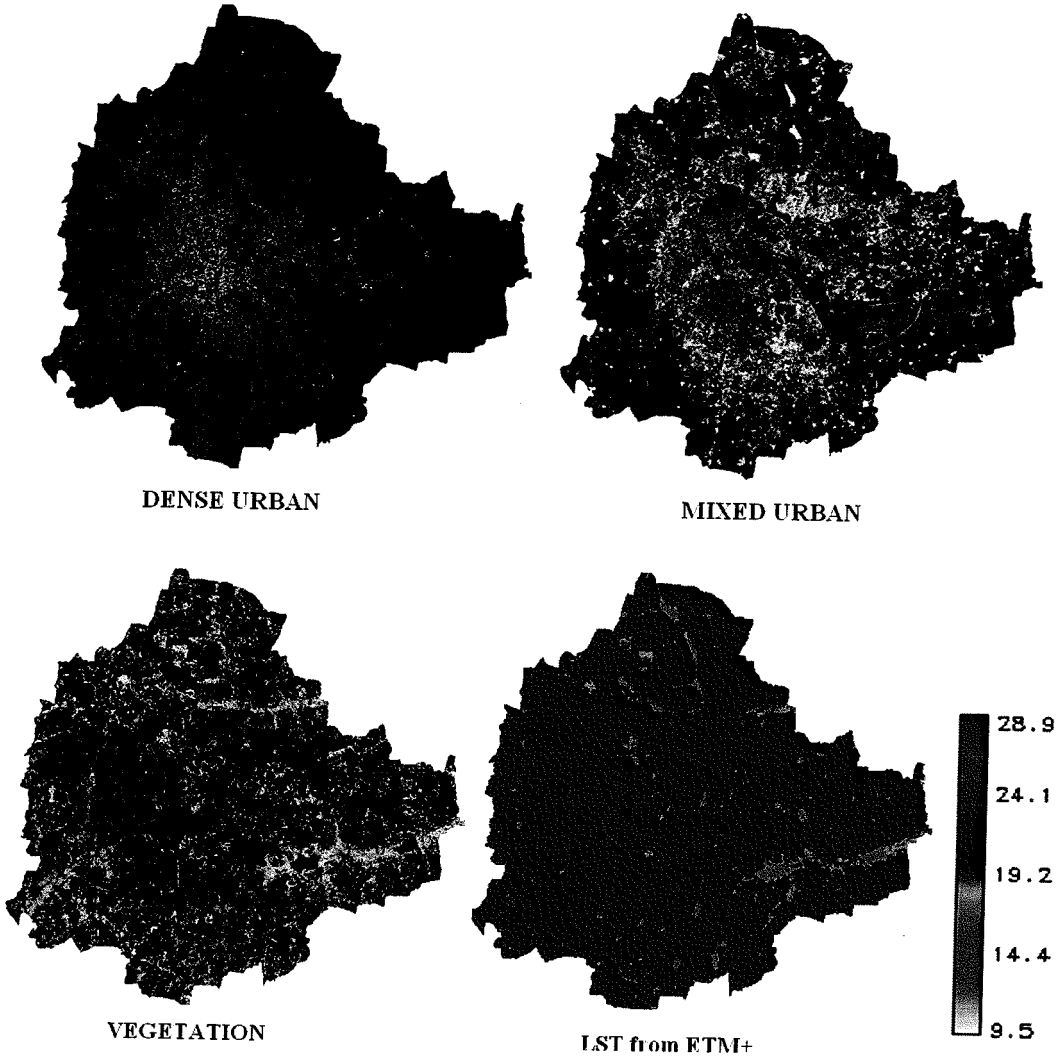

Figure 11. Abundance maps and LST obtained from Landsat ETM+ data.

The relationship between LST and NDVI was investigated for each LC type through the Pearson's correlation coefficient at a pixel level and are listed in table 8. The significance of each correlation coefficient was determined using a one-tail Student's t-test. It is apparent that values tend to negatively correlate with NDVI for all LC types. NDVI values for built up ranges from -0.05 to -0.6. Temporal increase in temperature with the increase in the number of urban pixels during 1992 to 2007 (63%) is confirmed with the increase in "r" values for the respective years. The NDVI for vegetation ranges from 0.15 to 0.6. Temporal analyses of the vegetation show a decline of 45%, which is reflected in the respective temperature increase and the respective 'r' values confirm the trend.

Table 8. Correlation coefficients between LST and NDVI by Land use type (p=0.05)

Land use	1992	2000	2007
Built up	-0.7188	-0.7745	-0.7900
Vegetation	-0.8720	-0.6211	-0.6071
Open ground	-0.6817	-0.5837	-0.6004
Water bodies	-0.4152	-0.4182	-0.4999

Relationship of Population Density with LST

The population data used in the analysis were from Census, 2000 coinciding with the acquisition of ETM+ data of 2000 from which LST were derived. Figure 12 provides the temperature profile for 100 wards with different population densities.

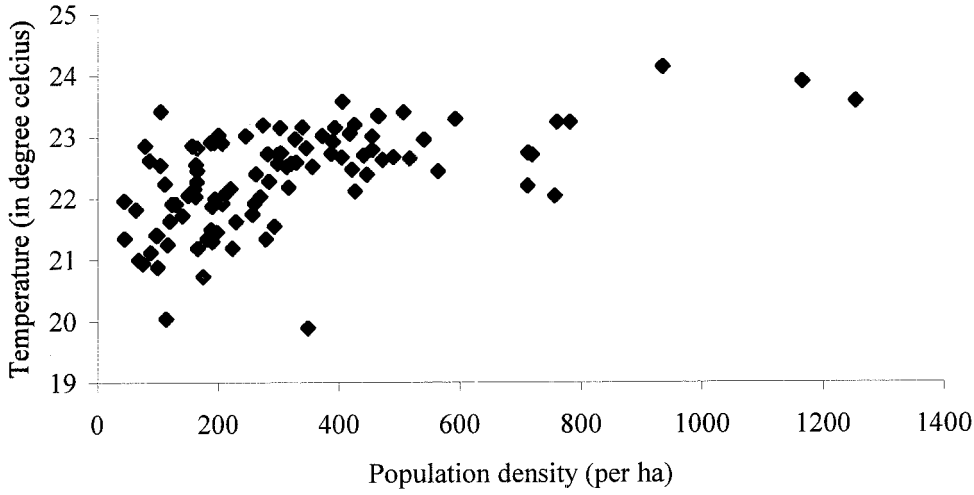

Figure 12. Ward wise temperature and population density

Increased urbanization has resulted in higher population densities in certain wards, which incidentally have higher LST due to higher level of anthropogenic activities, which corroborate with the reports for Fukuoka City, Japan (Tanaka *et al.*, 2005).

Effect of Different Land use Classes Derived from Combined Outputs of Unmixed Image and Bayesian Classification on Lst

The abundance output of the Landsat ETM+ images were combined with the signatures of the five classes that were collected from the ground and the Baye's classifier was used to obtain new improved land use map. The output of the unmixing algorithm controls the output of the Baye's classifier by providing the prior probability of each class for every pixel apart

from the training pixels. Given a set of multispectral images the computation is done as follows:

- The abundances of all categories in the data are computed using an unmixing algorithm discussed earlier. For each pixel, abundance of each category is used as a prior probability of the class.
- Let x denote the multispectral observation vector and k any class.
- In the Baye's classifier for the multispectral data, the posterior probability of the class given the observation is computed by multiplying the prior probability of the class (obtained from the unmixing algorithm) with the conditional probability P(x|k). The class label assigned to the pixel is

$$l = \arg\min_{k} \frac{P(k \mid i, j)P(x \mid k)}{P(x)} \tag{36}$$

In the conventional approach, the prior probability of all classes is assumed to be same for all pixels through out the image. This unmixing decision based approach, systematically exploits the information from both the sources for achieving more reliable classification. The output of this approach is shown in Figure 13. Table 9 shows the LST, NDVI and correlation coefficients land use wise.

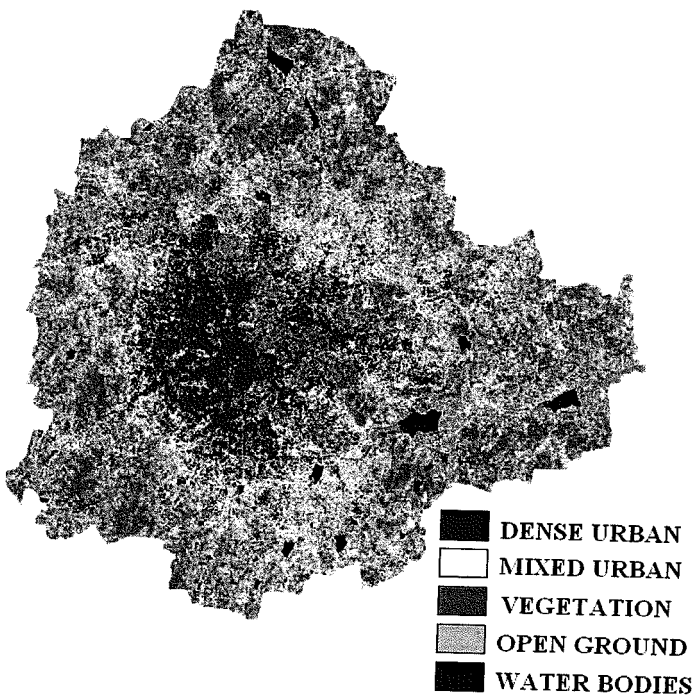

Figure 13. Classified image obtained from combining unmixed images and training data as input to Baye's classifier with 6 multispectral bands of Landsat ETM+

Table 9. LST, NDVI and correlation coefficient for different land use classes

Land use	LST (Mean±SD)	NDVI (Mean±SD)	Correlation coefficient between LST and NDVI
Dense built up	23.09±1.16	-0.2904±0.395	-0.7771
Mixed built up	22.14±1.06	-0.138±0.539	-0.6834
Vegetation	19.27±1.59	0.3969±0.404	-0.8500
Open Ground	22.40±1.97	-0.0193±0.164	-0.6319
Water Bodies	19.57±1.72	-0.301±0.47	0.2319

8 transacts were laid across the city in eight directions (north [N], north-east [NE], east [E], south-east [SE], south [S], south-west [SW], west [W] and north-west [NW]) as shown in Figure 14 and LST were analysed to understand the temperature dynamics in different directions. Table 10 gives the LST Mean and SD in various directions.

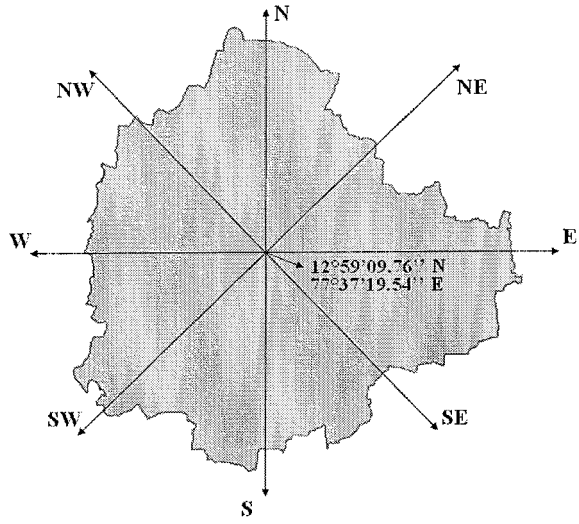

Figure 14. Transect lines superimposed on Greater Bangalore boundary

Table 10. LST across eight directions

Direction	Mean LST±SD
N	21.30±2.39
NE	22.15±2.22
E	21.01±2.47
SE	21.34±2.30
S	21.71±2.07
SW	22.19±1.92
W	22.97±1.72
NW	22.07±2.25

Temperature profile was further analysed by overlaying the LST map on the Baye's classified map to visualise the effect of different land uses. The temperature profile given in Figure 15, show that for vegetation patch or water body temperature fell below the mean on the transact (marked with circle) beginning from the center of the city and moving outwards along the transact. Regions in SW, W, N and NE coincides with urban growth poles (due to intense urbanisations consequent to setting up of IT corridors and industrial plots in the region; likely increase in urban pixels would be 48% in N, 51% in NE, 41% S and 38% in SE directions as listed in table 11).

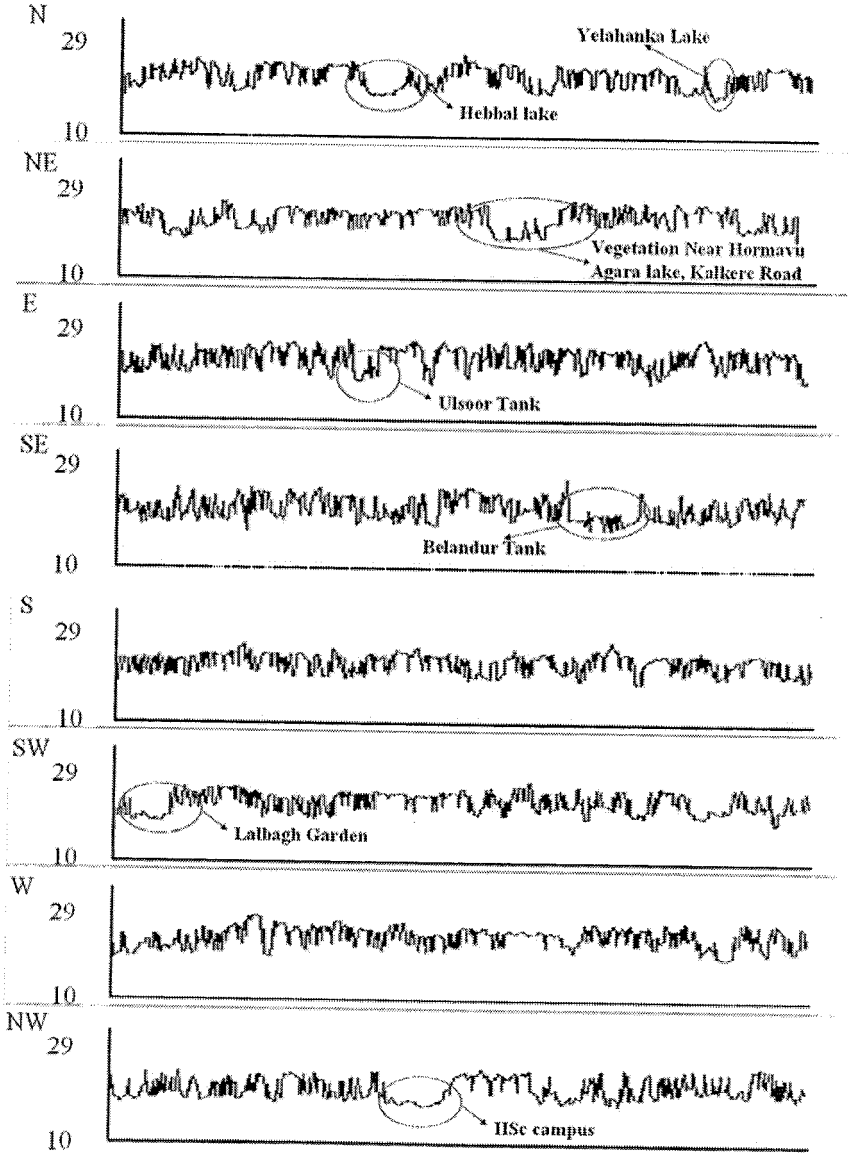

Figure 15. Temperature profile across N, NE, E, SE, S, SW, W and NW

(X axis – Movement along the transact from the city centre (see Fig. 14), Y axis - Temperature (°C))

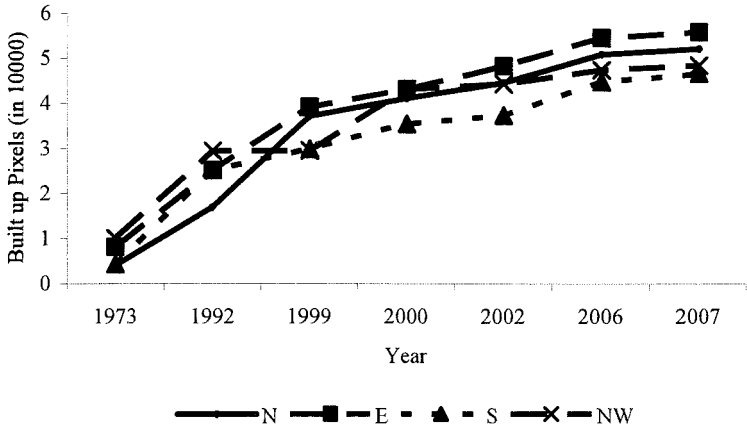

Figure 16. Temporal growth of built up pixels in various directions.

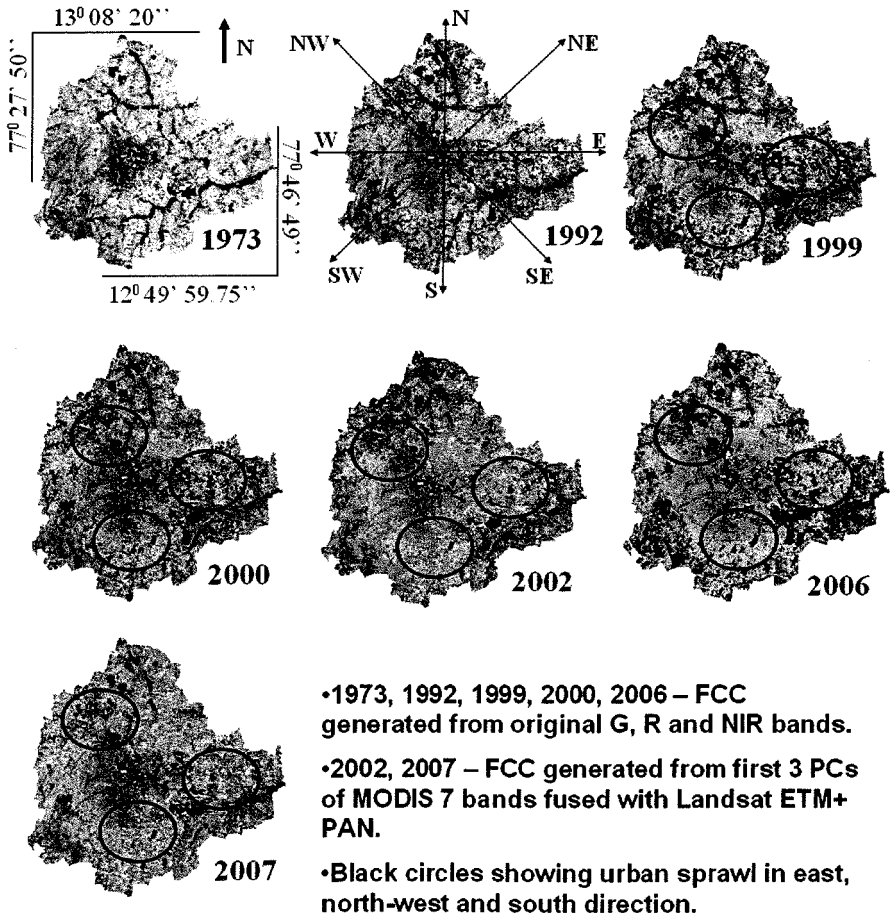

Figure 17. Temporal changes in built up area in Greater Bangalore (eight directions)

The dynamics of built up pixels from 1973 to 2007 in Greater Bangalore is presented in Figure 16. The growth poles are evident in Figure 17, which are false colour composites for 1973, 1992, 1999, 2000, 2002 and 2007 towards N, NE, S and SE indicating the intense urbanisation process due to growth agents like setting up of IT corridors, Peenya industrial units, etc. The growth in northern direction can be attributed to the new International Airport, encouraging other commercial and residential hubs. The southern part of the city is experiencing new residential and commercial layouts and the north-western part of the city outgrowth corresponds to the Peenya industrial belt along the Bangalore-Pune National Highway 4. The forecast of the growth of built up pixels in various directions for 2010, 2015 and 2020 are listed in table 11. Projected increase in urban pixels during the next 15 years would be 48% in N, 51% in NE, 41% S and 38% in SE directions.

Table 11. Projections of growth (built up pixels) 2010, 2015 and 2020

Direction	Equation	R^2	SE (ha)	Increase in Builtup Area (ha)		
				2010	2015	2020
N	y = 2E-64e0.0786x	0.98	505	7374	10924	16184
NE	y = 8E-69e0.0833x	0.97	383	3737	5668	8597
E	y = 7E-47e0.0585x	0.99	373	7343	9838	13180
SE	y = 1E-52e0.0648x	0.99	293	3313	4581	6334
S	y = 4E-57e0.0701x	0.97	244	5608	7963	11305
SW	y = 8E-22e0.0294x	0.99	58.3	3323	3849	4459
W	y = 1E-21e0.0294x	0.97	196	4154	4812	5573
NW	y = 8E-37e0.0468x	0.95	411	5135	6489	8200

CONCLUSION

Field verification showed that newly built up areas obtained from digital classification of remotely sensed data, had the maximum number of small-scale industries, IT companies, multistoried building and private houses that came up in the last one decade. However, to account for the micro-level study of the land use with a detailed growth model, the classification process would require further refinement with other techniques like bootstrap, a computer implementation of the nonparametric or parametric ML estimation that provide direct computational way of assessing uncertainty and estimates of standard errors (Hastie *et al.*, 2001) along with high spatial resolution data like IRS-1C PAN (with 5.8 m) or Cartosat-1/2 (with 2 m/1 m spatial resolution). Supervised learning seeks to extract information from labeled samples. If the underlying distribution comes from a mixture of component densities described by a set of unknown parameters Θ, then Θ can be estimated by ML methods. Pattern classifiers along with the advances in geo-informatics coupled with the availability of higher spatial, spectral and temporal resolution data help in extracting spatial features of interest like land cover classes such as built up. In this context, an important application of pattern classifiers would be to estimate accurate temporal land cover statistics that are useful in monitoring the status and extent of these features. The analysis showed a rapid growth of urban pockets and consequent decline of water bodies and vegetation in Greater Bangalore.

Shannon's entropy computed for Bangalore city for 2000 and 2006, (1.0325 and 1.0782) are closer to the upper limit of log n, i.e. 1.0986, showing the higher degree of dispersion of built-up in the city.

Urbanisation and the consequent loss of lakes has led to decrease in catchment yield, water storage capacity, wetland area, number of migratory birds, flora and fauna diversity and ground water table. Temporal analyses of waterbodies in Greater Bangalore indicate the decline of 32.47% during 1973 to 1992, 53.76% during 1973-2002 and 60.83% during 1973-2007 consequent to a linear growth of 466% of built up/urban area. As land is converted, it loses its ability to absorb rainfall. Urbanisation has increased runoff 2 to 6 times over what would occur on natural terrain in some pockets of Bangalore.

The relationship between LST and NDVI investigated through the Pearson's correlation coefficient at a pixel level and the significance tested through one-tail Student's t-test, confirms the relationship for all LC types. Also, increased urbanisation has resulted in higher population densities in certain wards, which incidentally have higher LST due to higher level of anthropogenic activities.

The growth poles are towards N, NE, S and SE of the city indicating the intense urbanisation process due to growth agents like setting up of IT corridors, Peenya industrial units, etc. The growth in northern direction can be attributed to the new International Airport, encouraging other commercial and residential hubs. The southern part of the city is experiencing new residential and commercial layouts and the north-western part of the city outgrowth corresponds to the Peenya industrial belt along the Bangalore-Pune National Highway 4. The forecast of the growth of built up pixels in various directions during the next 15 years would be 48% in N, 51% in NE, 41% S and 38% in SE directions.

SUMMARY

Urbanisation is the increase in the population of cities in proportion to the region's rural population. Urbanisation in India is very rapid with urban population growing at around 2.3 percent per annum. Urban sprawl refers to the dispersed development along highways or surrounding the city and in rural countryside with implications such as loss of agricultural land, open space and ecologically sensitive habitats. Sprawl is thus a pattern and pace of land use in which the rate of land consumed for urban purposes exceeds the rate of population growth resulting in an inefficient and consumptive use of land and its associated resources.

This unprecedented urbanisation trend due to burgeoning population has posed serious challenges to the decision makers in the city planning and management process involving plethora of issues like infrastructure development, traffic congestion, and basic amenities (electricity, water, and sanitation), etc. In this context, to aid the decision makers in following the holistic approaches in the city and urban planning, the pattern, analysis, visualization of urban growth and its impact on natural resources has gained importance. This communication, analyses the urbanisation pattern and trends using temporal remote sensing data based on supervised learning using maximum likelihood estimation of multivariate normal density parameters and Bayesian classification approach. The technique is implemented for Greater Bangalore – one of the fastest growing city in the World, with Landsat data of 1973, 1992 and 2000, IRS LISS-3 data of 1999, 2006 and MODIS data of

2002 and 2007. The study shows that there has been a growth of 466% in urban areas of Greater Bangalore across 35 years (1973 to 2007). The study unravels the pattern of growth in Greater Bangalore and its implication on local climate and also on the natural resources, necessitating appropriate strategies for the sustainable management.

REFERENCES

Artis, D. A., and Carnahan, W. H. (1982). Survey of emissivity variability in thermography of urban areas. *Remote Sensing of Environment* **12**: 13-329.

Arumugam, M., Emerson, C. W., Siu-Ngan Lam, N., and Quattrochi, D. A. (2003). Classifying urban land covers using local indices of spatial complexity. Proceedings of the ASPRS 2003 Annual Conference, Anchorage, AK, May 2003, CD-ROM.

Balling, R. C., and Brazell, S. W. (1988). High resolution surface temperature patterns in a complex urban terrain. *Photogrammetric Engineering and Remote Sensing* **54**: 1289-1293.

Barnsley, M. J., and. Barr, S. L. (1997). Distinguishing urban land-use categories in fine spatial resolution land-cover data using a graph-based, structural pattern recognition system. *Computers Environment and Urban Systems* **21**(3/4): 209-225.

Barr, S., and Barnsley, M. (2000). Reducing structural clutter in land cover classifications of high spatial resolution remotely-sensed images for urban land use mapping. *Computers & Geosciences* **26**: 433-439.

Becker, F., and Li, Z. -L. (1990). Temperature-independent spectral indices in TIR bands. *Remote Sensing of Environment* **32**: 17–33.

Berry, B. J. L. (1990). Urbanisation. In The Earth as Transformed by Human Action (B. L. Turner II, W. C. Clark, R. W. Kates, J. F. Richards, J. T. Mathews, and W. B. Meyer, eds.), Cambridge University Press, Cambridge, U. K. pp. 103-119.

Betts, A., Ball, J., Beljaars, A., Miller, M., and Viterbo, P. (1996). The land surface–atmosphere interaction: A review based on observational and global modeling perspectives. *Journal of Geophysical Research* **101**: 7209-7225.

Boegh, E., Soegaard, H., Hanan, N., Kabat, P., and Lesch, L. (1998). A remote sensing study of the NDVI–Ts relationship and the transpiration from sparse vegetation in the Sahel based on high resolution satellite data. *Remote Sensing of Environment* **69**: 224-240.

Campana, N. A. and Tucci, C. E. M. (2001). Predicting floods from urban development scenarios: case study of the Diluvio Basin, Porto Alegre, Brazil. *Urban Water* **3**: 113-124.

Carnahan, W. H., and Larson, R. C. (1990). An analysis of an urban heat sink. *Remote Sensing of Environment* **33**: 65-71.

Carper, W.J., Lilesand, T.W., and Kieffer, R.W. (1990). The use of intensity–hue–saturation transformation for merging SPOT panchromatic and multispectral image data. *Photogrammetric Engineering and Remote Sensing* **56(4)**: 459–467.

Carson, T. N., Gillies, R. R., and Perry, E. M. (1994). A method to make use of thermal infrared temperature and NDVI measurements to infer surface soil water content and fractional vegetation cover. *Remote Sensing Reviews* **9**: 161-173.

Compana, N. A., and Tucci, C. E. M. (1994). Estimativa de area Impermeavel de macro bacias urbanas. RBE, *Caderno de Recursos Hidricos* **12(2)**: 79-94.

Dash, P., Gottsche, F. -M., Olesen, F. -S., and Fischer, H. (2002). Land surface temperature and emissivity estimation from passive sensor data: Theory and practice-current trends. *International Journal of Remote Sensing* **23(13)**: 2563-2594.

Diaz, O., and Tucci, C. E. M. (1987). Regionalizacao de Hidrogramas Unitarios de Bacias Urbans. *Caderno de Recursos Hidricos Revista Brasileira de Engenharia* **7(2)**: 19-30.

Douglas I. (1994). Human Settlements. In: William B. Meyer and B.L. Turner II (Editors), Changes in Land Use and Land Cover: A Global Perspective. Cambridge University Press, Cambridge, U.K.

Duda, R. O., Hart, P. E., and Stork, D, G. (2000). *Pattern classification*, Wiley-Interscience Publication, New York (ISBN 9814-12-602-0).

Elena G. I., and Nancy E. B. (2004). Land use externalities, open space preservation, and urban sprawl. Regional Science and Urban Economics **34:** 705-725.

Franca, G. B., and Cracknell, A. P. (1994). Retrieval of land and sea surface temperature using NOAA-11 AVHRR data in north-eastern Brazil. *International Journal of Remote Sensing* **15**: 1695-1712.

Friedl, M. A. (2002). Forward and inverse modeling of land surface energy balance using surface temperature measurements. *Remote Sensing of Environment* **79**: 344-354.

Friedl, M. A., and Davis, F. W. (1994). Sources of variation in radiometric surface temperature over a tallgrass prairie. *Remote Sensing of Environment* **48**: 1-17.

Fukushima, K. (1988). A Neural Network for Visual Pattern Recognition, *IEEE Computer*, 65-74.

Gallo, K. P., and Owen, T. W. (1998) Assessment of urban heat island: A multi-sensor perspective for the Dallas-Ft. Worth, USA region. *Geocarto International* **13**: 35-41.

Gallo, K. P., McNab, A. L., Karl, T. R., Brown, J. F., Hood, J. J., and Tarpley, J. D. (1993) The use of NOAA AVHRR data for assessment of the urban heat island effect. *Journal of Applied Meteorology* **32**: 899-908.

Galster, G, Hanson, R, Ratcliffe, M R, Wolman, H, Coleman, S and Freihage, J. (2001). Wrestling sprawl to the ground: defining and measuring an elusive concept. *Housing Policy Debate* **12(4)**.

Gillespie, A. R. (1985). Lithologic mapping of silicate rocks using TIMS. Proceedings TIMS Data User's Workshop. JPL Publ., **86–38:** 29-44, Pasadena, CA: Jet Propulsion Laboratory.

Gillespie, A. R., Rokugawa, S., Matsunaga, T., Cothern, J. S., Hook, S. J., and Kahle, A. B. (1998). A temperature and emissivity separation algorithm for advanced spaceborne thermal emission and reflection radiometer (ASTER) images. *IEEE Transactions on Geoscience and Remote Sensing* **36**: 1113-1126.

Gillies, R. R., and Carlson, T. N. (1995) .Thermal remote sensing of surface soil water content with partial vegetation cover for incorporation into climate models. *Journal of Applied Meteorology* **34**: 745-756.

Gillies, R. R., Carlson, T. N., Cui, J., Kustas, W. P., and Humes, K. S. (1997). A verification of the 'triangle' method for obtaining surface soil water content and energy fluxes from remote measurements of the Normalized Difference Vegetation index (NDVI) and surface radiant temperature. *International Journal of Remote Sensing* **18**: 3145-3166.

Gluch, R. (2002). Urban growth detection using texture analysis on merged Landsat TM and SPOT-P Data. *Photogrammetric Engineering and Remote Sensing* **68**: 1283-1288.

Goetz, S. J. (1997). Multisensor analysis of NDVI, surface temperature and biophysical variables at a mixed grassland site. *International Journal of Remote Sensing* **18**: 71-94.

Gong, P., and Howarth, P. J. (1990). The use of structural information for improving land-cover classification accuracies at the rural–urban fringe. *Photogrammetric Engineering and Remote Sensing* **56**: 67-73.

Gori, M., and Scarselli, F. (1998). Are Multilayer Perceptrons Adequate for Pattern Recognition and Verification?, *IEEE Transactions on Pattern Analysis and Machine Intelligence* **20(11)**: 1121-1132.

Goward, S. N., Xue, Y., and Czajkowski, K. P. (2002). Evaluating land surface moisture conditions from the remotely sensed temperature/vegetation index measurements: An exploration with the simplified simple biosphere model. *Remote Sensing of Environment* **79**: 225-242.

Guindon, B., Zhang, Y., and Dillabaugh, C. (2004). Landsat urban mapping based on a combined spectral–spatial methodology. *Remote Sensing of Environment* **92**: 218-232.

Hastie, T., Tinshirani, R., and Friedman, J. (2001). *The Elements of Statistical Learning – Data Mining*, Inference, and Prediction, Springer, Canada.

Homer, C., Huang, C., Yang, L., and Wylie, B. (2002). Development of a Circa 2000 land cover database for the United States. Proceedings of the 2002 ASPRS Annual Convention, April 2002, Washington, DC, CD-ROM.

Kato, S., and Yamaguchi, Y. (2005). Analysis of urban heat-island effect using ASTER and ETM+ Data: Separation of anthropogenic heat discharge and natural heat radiation from sensible heat flux. *Remote Sensing of Environment* **99**: 44-54.

Kealy, P. S., and Gabell, A. R. (1990). Estimation of emissivity and temperature using alpha coefficients. Proceedings of Second TIMS Workshop. JPL Publ., **90– 95**: 11-15. Pasadena, CA: Jet Propulsion Laboratory.

Kidder, S. Q., and Wu, H. T. (1987). A multispectral study of the St. Louis area under snow-covered conditions using NOAA-7 AVHRR data. *Remote Sensing of Environment* **22:** 159-172.

Konig, A., Sægrov, S., and Schilling, W. (2002). Damage assessment for urban flooding, Ninth International Conference on Urban Drainage, Portland, Oregon, USA.

Kulkarni, V. and Ramachandra T.V. (2006). *Environmental Management*, Commonwealth Of Learning, Canada and Indian Institute of Science, Bangalore.

Kulkarni, V. and Ramachandra T.V. (2006). Environmental Management, Commonwealth Of Learning, Canada and Indian Institute of Science, Bangalore, Printed by Capital Publishing Company, New Delhi.

Kwan, H. K., and Cai, Y. (1994). A Fuzzy Neural Network and its Application to Pattern Recognition. *IEEE Transactions on Fuzzy Systems* **2(3)**: 185-193.

Lambin, E. F., and Ehrlich, D. (1996). The surface temperature– vegetation index space for land cover and land-cover change analysis. *International Journal of Remote Sensing* **17**: 463-487.

Landsat Project Science Office. (2002). Landsat 7 science data user's handbook. Goddard Space Flight Center, Available from: www.address: http://ltwww.gsfc.nasa.gov/IAS/handbook/ handbook_toc.html.

Lee, C. H. N., Liu, A., and Chen, W. S. (2006). Pattern Discovery of Fuzzy Time Series for Financial Prediction. *IEEE Transactions on Knowledge and Data Engineering* **18(5)**: 613-625.

Li, F., Jackson, T. J., Kustas, W, Schmugge, T., J., French, A. N., Cosh, M. L., and Bindlish, R. (2004). Deriving land surface temperature from Landsat 5 and 7 during SMEX02/SMACEX. *Remote Sensing of Environment* **92:** 521-534.

Lillesand, T.M. and Kiefer, R. W. (2002). Remote Sensing and Image Interpretation, Fourth Edition, John Wiley and Sons, New York. (ISBN 9971-51-427-3)

Masek, J. G., Lindsay, F. E., and Goward, S. N. (2000). Dynamics of urban growth in the Washington DC Metropolitan Area, 1973–1996, from Landsat observations. *International Journal of Remote Sensing* **21**: 3473-3486.

Masser, I., Cheng, J. (2003). Urban growth pattern modeling: a case study of Wuhan city, PR China. *Landscape and urban planning* **62**: 199-217.

Mesev, V. (2005). Identification and characterisation of urban building patterns using IKONOS imagery and point-based postal data. *Computers Environment and Urban system* **29**: 541-557.

Moller-Jensen, K. (1990). Knowledge-based classification of an urban area using texture and context information in Landsat-TM imagery. *Photogrammetric Engineering and Remote Sensing* **56**: 899-904.

Nancy, T., Chad, H., and Russell, G. C. (2003). A Comparison of Urban Mapping Methods Using High-Resolution Digital Imagery. *Photogrammetric Engineering & Remote Sensing* **69(9)**: 963-972.

Nichol, J. E. (1994). A GIS-based approach to microclimate monitoring in Singapore's high-rise housing estates. *Photogrammetric Engineering and Remote Sensing* **60**: 1225-1232.

Nikolakopoulos, K. G, Vaiopoulos, D. A, Skianis, G. A. (2003). Use of multitemporal remote sensing thermal data for the creation of temperature profile of Alfios river basin. *Geoscience and Remote Sensing Symposium, 21-25 July 2003, IGARSS '03. Proceedings,IEEE International* **4:** 2389-2391.

Oke, T. R. (1982). The energetic basis of the urban heat island. *Quarterly Journal of the Royal Meteorological Society* **108**: 1-24.

Owen, T. W., Carlson, T. N., and Gillies, R. R. (1998). An assessment of satellite remotely-sensed land cover parameters in quantitatively describing the climatic effect of urbanization. *International Journal of Remote Sensing* **19**: 1663-1681.

Pajares, G., and Cruz, J.M.D.L. (2004). A wavelet –based image fusion tutorial. *The Journal of the Pattern Recognition Society* **37**: 1855-1872.

Peiser, R. (2001). Decomposing urban sprawl. *Town Planning Review* **72(3)**: 275-298.

Phinn, S., Stanford, M., Scarth, P., Murray, A. T., and Shyy, P. T. (2002). Monitoring the composition of urban environments based on the Vegetation–Impervious surface–Soil (VIS) model by Subpixel Analysis Techniques. *International Journal of Remote Sensing* **23**: 4131-4153.

Porto, R.L., Zahel, F. K., Tucci,C. E. M., and Bidone, F. (1993). Drenagem Urbana. In C. E. M. Tucci (org), Hydrologia: Ciencia e Aplicacao (pp. 805-847). Editora da UFRGS, EDUSP, ABRH.

Prata, A. J., Caselles, V., Coll, C., Sobrino, J. A., and Ottle, C. (1995). Thermal remote sensing of land surface temperature from satellites: Current status and future prospects. *Remote Sensing Reviews* **12**: 175-224.

Quattrochi, D. A., and Goel, N. S. (1995). Spatial and temporal scaling of thermal remote sensing data. *Remote Sensing Reviews* **12**: 255-286.

Ramachandra, T. V., Jagadish, K. S., Sudhira, H. S., Raj, K. S., and Jha, S. K., Urban Sprawl Pattern Analysis Using GIS, CES Technical Report No. 99, Centre for Ecological sciences, Indian Institute of Science, Bangalore. http://wgbis.ces.iisc.ernet.in/energy/urban/

Ramachandra, T. V., Subramanian, D. K. and Joshi, N. V. (1999). Hydro electric resource assessment in Uttara Kannada district, Karnataka state, India. *Journal of Cleaner Production* **7(3):**195-211.

Rashed, T., Weeks, J. R., Gadalla, M. S., and Hill, A. G. (2001). Revealing the anatomy of cities through spectral mixture analysis of multispectral satellite imagery: A case study of the Greater Cairo Region, Egypt. *Geocarto International* **16**: 5-15.

Rawashdeh, S. A., and Saleh, B. (2006). Satellite Monitoring of Urban Spatial growth in the Amman Area, Jordan, *Journal of urban planning and development* Pp. 211-216.

Ridd, M. K. (1995). Exploring a V–I–S (Vegetation-Impervious surface– Soil) model for urban ecosystem analysis through remote sensing: Comparitive anatomy of cities. *International Journal of Remote Sensing* **16**: 2165-2185.

Roth, M., Oke, T. R., and Emery, W. J. (1989). Satellite derived urban heat islands from three coastal cities and the utilisation of such data in urban climatology. *International Journal of Remote Sensing* **10**: 1699-1720.

Sandholt, I., Rasmussen, K., and Andersen, J. (2002). A simple interpretation of the surface temperature/vegetation index space for assessment of surface moisture status. *Remote Sensing of Environment* **79**: 213-224.

Schmitt, T.G., Schilling,W., Sægrov, S. and. Nieschulz, K.-P. (2002). Flood risk management for urban drainage systems by simulation and optimisation, Ninth International Conference on Urban Drainage, Portland, Oregon, USA.

Schmugge, T., Hook, S. J., and Coll, C. (1998). Recovering surface temperature and emissivity from thermal infrared multispectral data. *Remote Sensing of Environment* **65**: 121-131.

Shi, P-J., Yuan, Y., Zheng, J., Wang, J-A., Ge, Yi., and Qiu, G-Y. (2007). The effect of land use/cover change on surface runoff in Shenzhen region, China. *Catena* **69**: 31-35.

Singh, S., M. (1998). Brightness Temperatures Algorithms of Landsat Thematic Mapper Data. *Remote Sensing of Environment* **24**: 509-512.

Snyder, W. C., Wan, Z., Zhang, Y., and Feng, Y. -Z. (1998). Classification based emissivity for land surface temperature measurement from space. *International Journal of Remote Sensing* **19**: 2753-2774.

Sobrino, J. A., and Raissouni, N. (2000). Toward remote sensing methods for land cover dynamic monitoring: Application to Morocco. *International Journal of Remote Sensing* **21**: 353-366.

Stathopoplou, M., Cartalis, C. and Petrakis, M. (2006). Integrating CORINE land cover data and landsat TM for surface emissivity definitions: an application for the urban area of Athens, Greece, *International Journal of Remote Sensing* **28(15):** 3291-3304.

Stathopoulou, M., and Cartalis, C. (2007). Daytime urban heat island from Landsat ETM+ and Corine land cover data: An application to major cities in Greece. *Solar Energy* **81**: 358-368.

Streutker, D. R. (2002). A remote sensing study of the urban heat island of Houston, Texas. *International Journal of Remote Sensing* **23**: 2595-2608.

Sudhira H.S., Ramachandra T.V., Bala Subramanya M.H. (2007). City Profile: Bangalore., *Cities* **124(4)**: 379-390.

Sudhira, H.S., Ramachandra, T.V., and Jagadish, K. S. (2003). Urban sprawl: metrics, dynamics and modelling using GIS, *International Journal of Applied Earth Observation and Geoinformation* **5(2004)**: 29-39.

Tanaka, Y.; Shibata, S.; Gotoh, K. (2005). Appearance characteristic analysis of Heat Island phenomenon by using satellite remote sensing and GIS. *Geoscience and Remote Sensing Symposium*, 25-29 July 2005, IGARSS '05, Proceedings, IEEE International, **3**: 1855-1858.

Tian, G., Liu, J., Xie, Y., Yang, Z., Zhuang, D., and Niu, Z. (2005). Analysis of spatio temporal dynamic pattern and driving forces of urbanland in China in 1990s using TM images and GIS. *Cities* **22(6)**: 400-410.

Valor, E., and Caselles, V. (1996). Mapping land surface emissivity from NDVI: Application to European, African, and South American areas. *Remote Sensing of Environment* **57**: 167–184.

Walsh, S. J., Moody, A., Allen, T. R., and Brown, D. G. (1997). Scale dependence of NDVI and its relationship to mountainous terrain. In D. A. Quattrochi, and M. F. Goodchild (Eds.), Scale in Remote Sensing and GIS, pp. 27-55, Boca Raton, FL: Lewis Publishers.

Wang, J. (1993). LINDA—a system for automated linear feature detection and analysis. *Canadian Journal of Remote Sensing* **19**: 9 – 21.

Watson, K. (1992). Spectral ratio method for measuring emissivity. *Remote Sensing of Environment* **42**: 113-116.

Weng, Q. (2001). A remote sensing-GIS evaluation of urban expansion and its impact on surface temperature in the Zhujiang Delta, China. *International Journal of Remote Sensing* **22**: 1999-2014.

Weng, Q. (2003). Fractal analysis of satellite-detected urban heat island effect. *Photogrammetric Engineering and Remote Sensing* **69**: 555-566.

Weng, Q., Lu, D., and Schubring, J. (2004). Estimation of land surface temperature – vegetation abundances relationship for urban heat island studies. *Remote Sensing of Environment* **89**: 467-483.

World Urbanization Prospects. (2005). Revision, Population Division, Department of Economic and Social Affaris, UN.

Yang, L., Huang, C., Homer, C. G., Wylie, B. K., and Coan, M. J. (2003). An approach for mapping large-area impervious surfaces: Synergistic use of Landsat-7 ETM+ and high spatial resolution imagery. *Canadian Journal of Remote Sensing* **29**: 230– 240.

Yeh and Li, 2001. A.G.O. Yeh and X. Li. (2001). Measurement and monitoring of urban sprawl in a rapidly growing region using entropy. *Photogrammetry. Engineering and Remote Sensing* 67**(1)**: 83.

Yu, X. J., and Ng, C. N. (2007). Landscape and urban planning. Spatio and temporal dynamics of urban sprawl along two urban-rural transects: A case study of Guamgzhou, China **79**: 96-109.

Zha, Y., Gao, J., and Ni, S. (2003). Use of normalized difference built-up index in automatically mapping urban areas from TM imagery. *International Journal of Remote Sensing* **24**: 583-594.

Zhang, Q., Wang, J., Peng, X., Gong, P., and Shi, P. (2003). Urban built-up land change detection with road density and spectral information from multi-temporal Landsat TM data. *International Journal of Remote Sensing* **23**: 3057-3078.

Question Bank

Fill in the Blanks

(1) Urban sprawl is _____.
(2) Urbanisation is _____.
(3) Urban population is increasing at _____ % per annum and ___ % population resides in urban India.
(4) Remote sensing data is useful in _____ _____ management.
(5) Consequences of urbansiation are _____, _____, _____, etc.
(6) Spatial resolution of Landsat MSS data (1973) is _____ and MSS data (1999) is _____.
(7) Accuracy assessment of a classified image is done using _____/_____ matrix and generally _____, _____, _____ accuracy are used to define the accuracy of each class.
(8) Reflectance for vegetation is maximum in _____ band.
(9) _____, _____, _____ are the three different types of resampling techniques.
(10)_____ classification technique works on neurons whereas _____ classification technique is based on the principle of genetics.
(11)_____ is the procedure that is used to assign coordinate system to each pixel in the image.
(12)Mixture of red and green produces _____, green and blue produces _____, blue and red produces _____and mixture of red, green and blue produces _____ colour.
(13)_____ is often used to remove data redundancy and also used in image fusion.
(14)_____ is a hyperspectral sensor.
(15)UTM stands for _____ _____ _____. It is divided into _____ zones. India lies in UTM zone _____.

State True or False

(1) The most important constraints of pixel-based image classification are that it results in spectral classes and each pixel is assigned to one class only.
(2) In the classification process a spectral class may be represented by several training classes.
(3) Thermal remote sensing is not based on the measuring of electromagnetic radiation in the infrared region of the spectrum.
(4) Principal Components represents maximum variability of the original datasets.

(5) In RGB-HIS algorithm, I is replaced by low resolution panchromatic data.
(6) Landsat TM and ETM+ have the same spatial resolution for thermal bands.
(7) Digital elevation model gives the elevation and presents a 3-D view of the terrain.
(8) Tone, shape, size, pattern, texture, site and association are the keys used in visual interpretation of remote sensing data.
(9) After resampling the shape of the image changes.
(10) Two different images can be fused without georeferencing.

Short Answer Questions

(1) What are the different types of urban sprawl?
(2) How the analysis of urban sprawl pattern help regional planning?
(3) How geoinformatics helps in optimal management of natural resources?
(4) List out and discuss briefly the impacts of urbanisation in a developing country like India?
(5) How does urban study help in minimising the environmental impacts of urbanisation?
(6) Do you think urbanisation is important? If answer is yes, then how one can achieve sustainable development with urbanisation.
(7) What is the difference between land use and land cover?
(8) What is false colour composite (FCC) and true colour composite? How does FCC help in image interpretation? You are shown a picture in which grass looks green and houses are red- what is your conclusion? Now, you are shown a picture in which grass shows purple and houses are black – what is your conclusion now?
(9) What information is contained in a histogram of image data?
(10) How many possibilities are there to visualize a 4 band image using a computer monitor?
(11) What is Principal component analysis? How is it useful? Can it be applied in any braches of science? Explain with an example?
(12) What is data fusion? List any 3 techniques of data fusion.
(13) Explain the difference between supervised and unsupervised classification?
(14) Define endmember. List any 3 techniques of endmember extraction and explain them briefly.
(15) State Baye's Theorem. What is Bayesian classifier? How is it dependent on conditional probability?

Long Answer Questions

(1) Differentiate between urbanisation and urban sprawl?
(2) What is the principal behind NDVI? How does NDVI help in discriminating vegetation, built up, water bodies? Explain.
(3) What is geometric correction and resampling? Why the images should be geometrically corrected. Explain in detail?

(4) What is digital image classification? Explain one classification technique (algorithm) in detail?

(5) What is Linear unmixing? How is this different from hard classification technique such as Baye's classifier?